論文 / 著書情報
Article / Book Information

題目(和文)	次世代通信応用に向けたGHz–THz帯におけるガラス材料の誘電応答に関する研究
Title(English)	Study on dielectric response of glass materials in GHz–THz band for next generation communication applications
著者(和文)	金原一樹
Author(English)	Kazuki Kanehara
出典(和文)	学位:博士(工学), 学位授与機関:東京工業大学, 報告番号:甲第12717号, 授与年月日:2024年3月26日, 学位の種別:課程博士, 審査員:保科 拓也,中島 章,矢野 哲司,松下 伸広,岸 哲生
Citation(English)	Degree:Doctor (Engineering), Conferring organization: Tokyo Institute of Technology, Report number:甲第12717号, Conferred date:2024/3/26, Degree Type:Course doctor, Examiner:,,,,
学位種別(和文)	博士論文
Category(English)	Doctoral Thesis
種別(和文)	要約
Type(English)	Outline

DOCTORAL THESIS

Study on dielectric response of glass materials in GHz–THz band for next generation communication applications

Kazuki Kanehara

Tokyo Institute of Technology

The School of Materials and Chemical Technology

Department of Materials Science and Engineering

Study on dielectric response of glass materials in GHz–THz band for next generation communication applications

by

Kazuki Kanehara

Submitted to the School of Materials and Chemical Technology
Department of Materials Science and Engineering
at the
TOKYO INSTITUTE OF TECHNOLOGY
March 2024

Author..
Kazuki Kanehara
Department of Materials Science and Engineering

Certificated by ....
Associate Professor Takuya Hoshina
Professor Tetsuji Yano
Professor Akira Nakajima
Professor Nobuhiro Matsushita
Associate Professor Tetsuo Kishi

Contents

Abstract

In recent years, fifth-generation (5G) communication systems have been developed to enable high-speed data exchange. The current systems typically use sub-6 bands, which are frequency bands below 6 giga hertz (GHz) ; although 5G systems currently use the sub-6 band, future technologies beyond 5G and sixth-generation (6G) systems will necessitate the use of higher-frequency bands exceeding 100 GHz. However, no suitable material has yet been found for communication substrates that operate well at frequencies above 100 GHz. Glass material is a candidate material with high flatness, heat resistance and rigidity as a material to realize 6G communication systems. On the other hand, the dielectric properties in the GHz band and the dielectric properties in the THz band, which affect the dielectric properties in the GHz band, have not been fully investigated. The dielectric properties of the THz band have not been fully investigated for a variety of materials, not only glass materials. This is because electromagnetic waves in the 100 GHz to 10 THz band have a high frequency to be measured as radio waves, but low energy to be measured as light, making them difficult to handle. In this study, I attempted to establish a measurement system for complex permittivity in the terahertz band, which is difficult to measure. In addition, the dielectric properties of glass materials in the GHz-THz band were investigated. They also worked on a prototype of a filter device, which is expected to be used as a substrate material.

In Chapter 1, I show some background on this study, the demand for high-speed communication systems and previous research on the dielectric properties of glass. The overall structure of this paper is presented. In Chapter 2, I introduce a novel THz ellipsometer to measure the dielectric properties in the THz band. The complex

permittivity of $SrTiO_3$ single crystal that was measured by the developed equipment showed good agreement with the complex permittivity obtained by analysis using the harmonic oscillator model. The combination of THz-TDS and ellipsometry has also made it possible to understand broadband dielectric dispersion in glass materials. This system enabled us to measure the complex permittivity in the THz band.

In Chapter 3, I discuss the effect of network modifiers on the GHz-THz dielectric properties of glass. Measurements of the dielectric properties of glasses in the THz band and molecular dynamic simulations have indicated that the dielectric dispersion of alkali silicate glasses is caused by the vibration and migration of alkali ions in the glass. Our experiments showed that the dielectric loss in the GHz band can be lowered by reducing the amount of alkali metal ions in the glass and including lighter alkali metal ions. The effect of alkaline earth metal ions on the dielectric constant was almost the same as that of alkali metal ions. Although alkaline earth metal ions exhibited a significantly small effect on the increase in dielectric loss, they also exhibited a limited effect on lowering viscosity; therefore, they are more suitable for moderately controlling the network modifier.

The dielectric properties of soda silicate glass with Al or B and aluminoborosilicate glass with alkaline earth metal ions were investigated and these results are presented in Chapter 4. The measurement results indicated that the dielectric loss in the low-frequency band is higher when Al is the network former, while the dielectric loss in the low-frequency band remains almost the same when B is the network former. This difference is due to the fact that when Al and B act as network formers in the glass, the peak frequency of the dielectric loss of the glass changes in the opposite direction.

Subsequently, I developed a substrate material with low temperature dependence of dielectric constant to obtain filter devices with low temperature dependence, whose details are presented in Chapter 5. To obtain glass material with low temperature dependence of dielectric constant, rutile crystals were deposited in glass. A glass-ceramic substrate with low temperature dependence of dielectric constant was developed, and a filter device for the 30 GHz frequency band was fabricated using the resulting substrate. Consequently, the filter device operated at a frequency of 30 GHz, and the temperature dependence was observed to be significantly small.

In this study, the origin of dielectric loss in glass materials for beyond 5G and 6G bands was investigated, glass material design guidelines were established, and the use of MSL filter devices using the resulting substrate was demonstrated. I believe that our result from this research can support future high-speed communication technologies.

Chapter 1

General Introduction

1.1 Expansion of high-speed communication technology

In recent years, fifth-generation (5G) communication systems are being increasing used worldwide owing to their numerous advances. The 5G communication systems can instantaneously treat significant amounts of data by using high-frequency bands. It is a communication technology that achieves ultra-high speed, low latency, and multiple simultaneous connections, and has a large social impact. In particular, low latency and multiple simultaneous connections are important features for the Internet of Things, which connects networks to all devices and stores large amounts of data. To further improve communication performance, high-frequency communications exceeding 100 GHz, such as "Beyond 5G" and "sixth-generation (6G) ", are expected, in the future.[1, 2] Radio wave reception and signal processing are important steps for achieving high-frequency band communication systems.

1.2 Characteristics required for substrate materials for high-frequency communication systems

High-frequency radio waves are highly directional and attenuated by the atmosphere. Therefore, the establishment of Beyond 5G and 6G systems requires the installation of a large number of base stations and receivers. Since a lot of radio wave transmitting and receiving devices will be required, the importance of the substrate material is more critical than for conventional communication devices. Against this background, various characteristics are required of substrate materials. The most important property required is low loss in the transmission of radio waves. A substrate material that reduces losses in the transmission of radio waves is a material with low dielectric loss and high quality flatness. The lower the dielectric loss of the substrate material, the better, since dielectric loss is a loss factor when signals are transmitted through the material. Suitable dielectric materials must also have high surface quality to minimize the skin effect, which implies that the current density is high near the surface of the conductor such that conduction loss increases at high frequencies.[3] If the surface roughness of the material is low, the current will flow a short distance, resulting in smaller losses during transmission. Dielectric constant is another important parameter required for substrate materials. The dielectric constant determines the electrode pattern and device size. A significantly high dielectric constant results in a considerably small device size, which increases the difficulty in drawing electrode patterns. Conversely, a significantly low dielectric constant results in a large device becomes, which is unsuitable for applications such as mobile devices.[4] Therefore, the dielectric constant must be controlled in the range of approximately 5–10. The cost of material fabrication is also important. As mentioned earlier, a large number of substrates are needed, so if the price of substrate materials is high, it will not be possible to create the infrastructure to build a communication system.

However, a material satisfying these characteristics is difficult to obtain. For example, fluorine resin materials have low dielectric constant and dielectric loss but have low Young's modulus and heat resistance, limiting their use as devices. Conversely, certain inorganic materials exhibit high Young's modulus and thermal resistance with significantly low dielectric loss in the 6G band. An important inorganic material is low-temperature co-fired ceramic (LTCC). LTCC filters,[5, 6] which consist of dielectric materials and metal MSLs, exhibit significant potential as alternative filter devices. However, the surface roughness of LTCC is in the range of a few micrometers. This flatness is too rough to obtain low electric resistance in the high-frequency band. Other candidate materials include single-crystal substrates. For example, single-crystal substrates of alumina have low loss, high flatness, and high heat resistance. However, the high price per substrate due to its single-crystal nature makes it unsuitable for practical use. Glass and crystallized glass substrates are attracting attention as materials that can satisfy all of these required characteristics. Therefore, the materials to be used for communications in the Beyond 5G and 6G bands have not yet been determined.

1.3 Investigation of complex permittivity of glass materials in the GHz-THz band

Glass is a suitable material for Beyond 5G or 6G communication systems owing to its thermal resistance, high quality flatness, high Young's modulus and cost.[7–10] However, the dielectric loss of glass material in the GHz range would not be investigated sufficiently. Figure 1-1 shows the Dielectric property of inorganic material in giga hertz to peta hertz band.[11] Because the dielectric property of inorganic material in GHz band is significantly affected by the dielectric property in THz band, the measurement of dielectric property in the GHz–THz band is important. However, only few reports exist on the dielectric property of glass in the GHz–THz band owing to the challenges in measuring the dielectric properties of glass in this range.[12, 13] This is because it is difficult to measure the complex permittivity in the GHz-THz band for all inorganic materials, not just glass materials. Figure 1-2 shows the method used to measure the complex permittivity in each frequency band. The band below the GHz band has been measured by impedance analyzers and has been the subject of many studies.[14, 15] On the other hand, in the GHz band, a vector network analyzer is used to make measurements.[16, 17] For example, dielectric properties are generally measured using the cavity resonator method or the SPDR method. On the other hand, it is difficult to measure complex dielectric properties in the bandwidth of about 100 GHz, and the BCDR and free space methods are used. However, even with these methods, the limit frequency of measurement is about 110 GHz. In recent years, various methods have been proposed to measure higher frequency bands with the aim of utilizing the 6G band; however, the limiting frequency of the technique is currently around 300 GHz.[18]

In contrast, the complex permittivity at THz frequencies is generally determined via infrared transmittance and reflectance. However, the infrared transmittance of inorganic materials is sometimes too low to accurately estimate the transmittance. The Kramers–Kronig transformation or lattice vibration analysis, which is useful for the analysis of crystals, cannot be easily applied for amorphous materials.[19–23] Despite the difficulty measuring dielectric properties in the THz band, Kamitsos *et al.* have been working vigorously on this subject. For example, they have calculated the infrared absorption coefficient in the THz band in borate glass from reflectance measurements using the Kramers–Kronig transformation and discussed the glass structure from the infrared absorption coefficient of glass.[21, 23–30] However, the Kramers–Kronig transformation determines the reflectance spectra over the entire frequency range, making it difficult to obtain absolute values. Kamitsos *et al.* discussed the measurement of infrared reflection or absorption; however, currently, only a few examples of measurements of complex permittivity exist, and the discussion was insufficient.[31, 32] Moreover, Mori *et al.* recently measured the complex permittivity of glass in the 0.5–3 THz band using THz-time-domain spectroscopy (THz-TDS).[33–37] Mori *et al.* primarily discussed the detection of boson peak. The boson peak is a vibration mode that is unique to glass, and has been observed in a few THz frequency ranges using Raman spectroscopy with low-temperature specific heat, inelastic neutron scattering, and infrared spectroscopy.[38–42] However, prior research[34, 43] indicates that the boson peak has a minimal effect on the dielectric properties at room-temperature conditions at frequencies beyond 5G and 6G. From these discussions, the complex permittivity at frequencies above 3 THz cannot be easily measured, and few examples of complex permittivity measurements in the THz band. However, the origin of the dielectric properties of glass materials in the GHz–THz band is still unclear.

On the other hand, dielectric properties in the GHz-THz band have been estimated in a form other than dielectric loss in previous studies. For example, Cai *et al.* attempted to understand the dielectric properties in the GHz band by measuring the complex permittivity below the GHz frequencies.[44] Lanagan *et al.* also introduced an equation to predict the dielectric constant of glass in the GHz range using the Clausius–Mossotti relation, as glass has no permanent dipole moment.[45, 46] J. M. Stevels *et al.* meaasured the conductivity of glass, and state that ions oscillate as network modifiers in the GHz-THz band.[47] H. Jain *et al.* also pointed out the possibility of site-to-site exchange of ions in the GHz band and the Jellyfish move, a phenomenon in which the entire glass network structure is shaken.[48] However, it could not be confirmed whether such atomic motion is really occurring in the GHz-THz band. There was also no quantitative understanding of how the movement of atoms in the GHz-THz band affects dielectric properties. Thus, clues to understanding the dielectric properties of glasses in the GHz-THz band have been studied, but it has not been possible to visualize how the dielectric properties change when the composition is changed, nor the movement of ions, the origin of the dielectric properties.

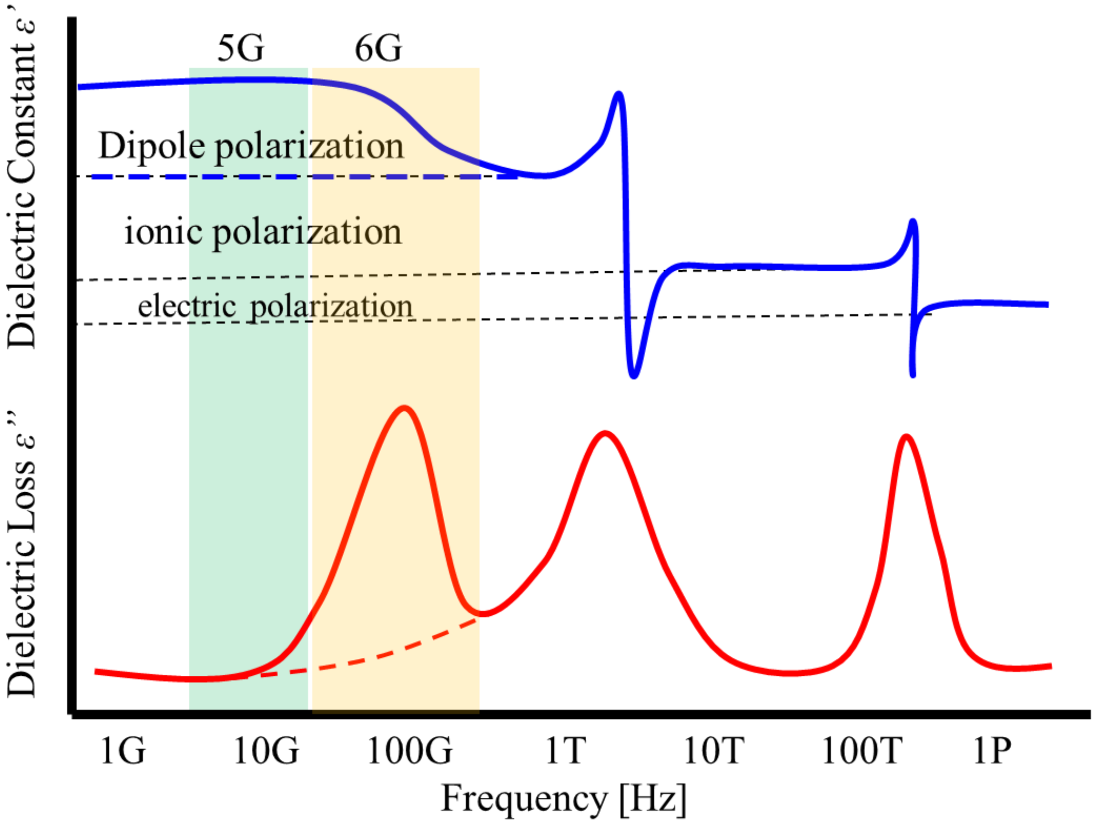

Figure 1-1 The Dielectric property of inorganic material in giga hertz to Peta hertz band

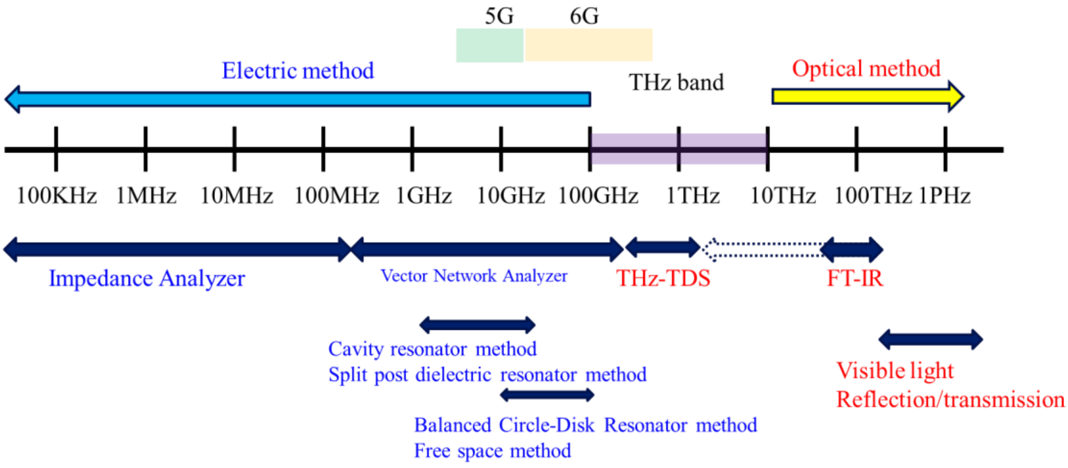

Figure 1-2 The method used to measure the complex permittivity in each frequency band.

1.4 Glass materials whose dielectric properties should be investigated

Since glass materials are materials that can contain a variety of elements, it is difficult to conduct research on all glass materials. Therefore, in this study, I mainly focused on silicate glass. Silicate glass is a glass material composed mainly of SiO_2, which can be manufactured inexpensively due to its high Clark number, and has a variety of industrial applications. Considering the constituents of glass, there are two types of oxides: network former oxides and network modifier oxides. In this study, I investigated the effects of several typical reticulation-forming oxides and modified oxides on the complex permittivity in the GHz-THz band, with silica as the major oxide, and explored their potential as glass material substrates.

1.5 Applications with suitable substrate materials for Beyond 5G 6G band filter devices

If suitable dielectric materials for Beyond 5G and 6G communications are developed, various applications can be considered, one of which is filter devices. Radio wave reception and signal processing are important steps for achieving high-frequency band communication systems. To effectively receive and process radio signals, four components wideband low-noise amplifier, radio frequency switch, radio frequency filters, and antenna switch, must be continuously updated.[49] Among these devices, I focused on filter devices in this research. Filters are devices that enable communication only at specific wavelengths and exhibit the characteristics shown in Figure 1-3. Surface acoustic wave (SAW) filters[50, 51] (Figure 1-4) and thin-film bulk acoustic resonator (FBAR) filters[52, 53] (Figure 1-5) are high-frequency filters that distinguish and pass signals in the required frequency bands for fourth-generation or 5G systems; however, these devices are unusable in the 6G band, that is above the W band (75–110 GHz).[54] The high-precision fabrication of SAW filters for bands over 10 GHz is challenging because the electrode spacing must be in the order of nanometers.[55] FBAR filters for the millimeter-wave band are difficult to obtain because the films need to be stacked in the order of several nanometers.[56] Microstrip line (MSL) and substrate-integrated waveguide (SIW) filters have also attracted attention as alternative filter devices.[57] An SIW filter (Figure 1-6) comprises several holes in the substrate and a circuit is drawn on it. An MSL filter (Figure 1-7) is composed of multiple electrodes arranged at specific intervals. Both filters exhibit advantages and disadvantages; however, the SIW filter is expensive because of the large number of holes required on the substrate and the need to maintain accuracy. In this study I focused on the MSL filter. When using a substrate as a material for a MSL filter, it is important to have a low temperature dependence of the dielectric constant in addition to the characteristics described in 1.2. This is because if the dielectric constant changes with temperature, the operating frequency of the filter will change, and the filter will not have the desired bandwidth.

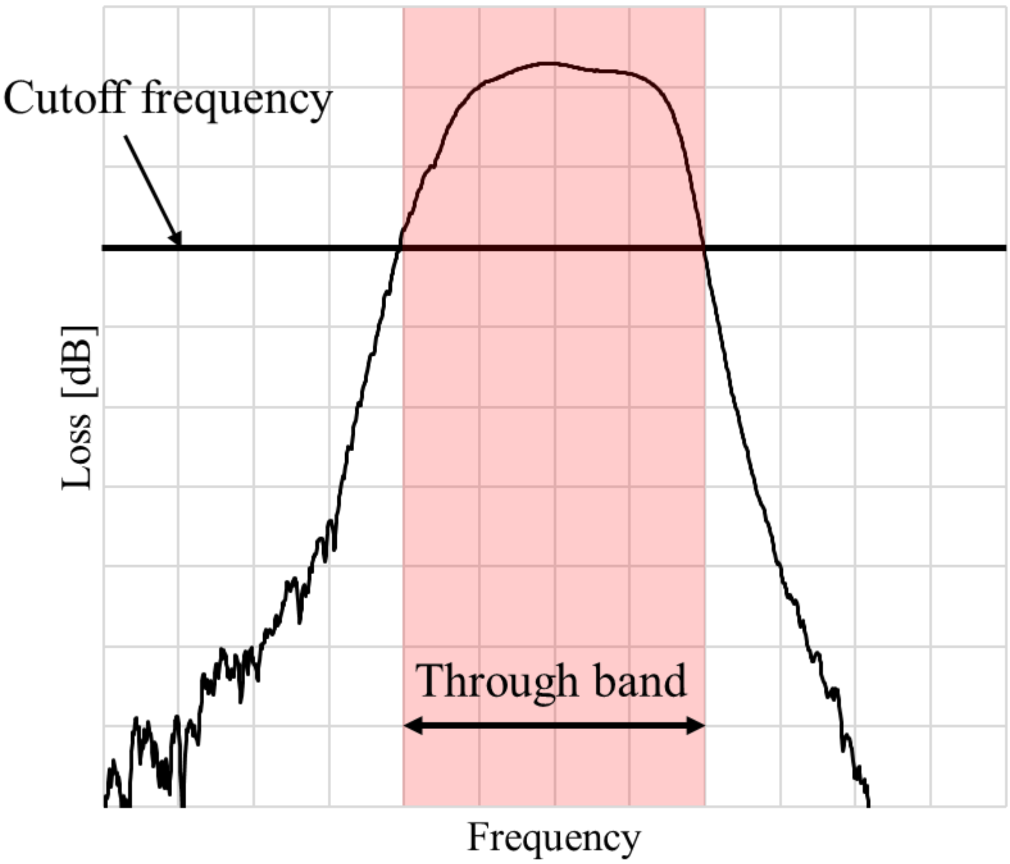

Figure 1-3 Schematic diagram of filter device performance

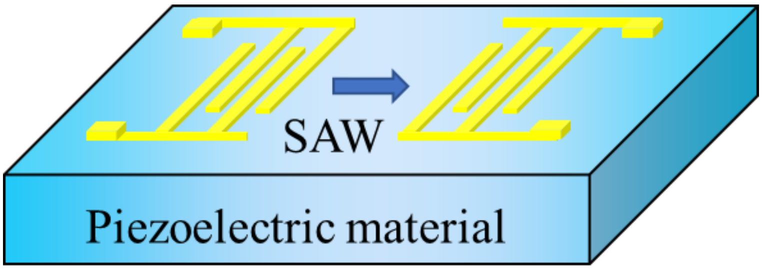

Figure 1-4 Schematic diagram of surface-acoustic-wave-type filter device

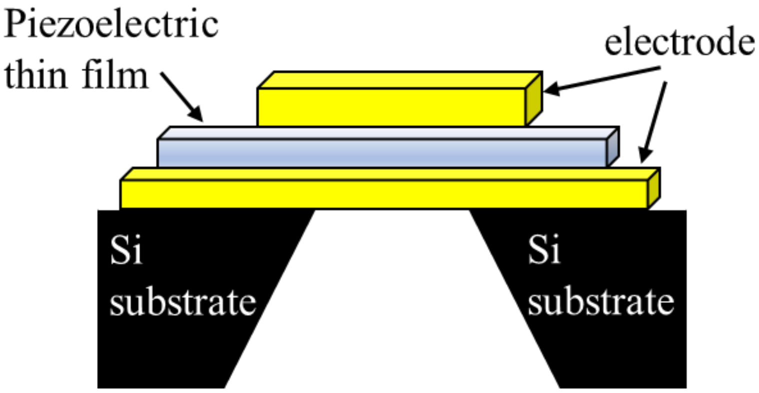

Figure 1-5 Schematic diagram of thin-film bulk acoustic resonator-type filter device

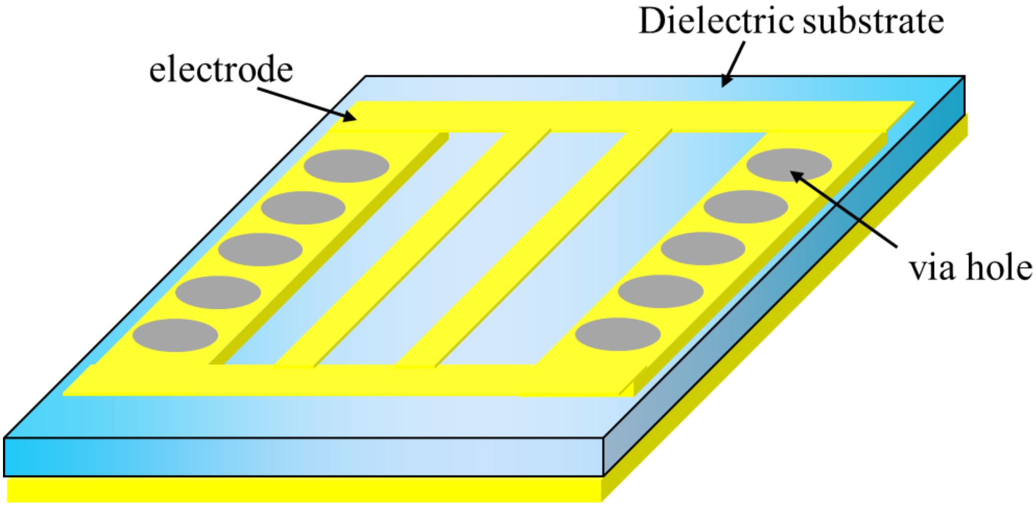

Figure 1-6 Schematic diagram of substrate-integrated waveguide-type filter device

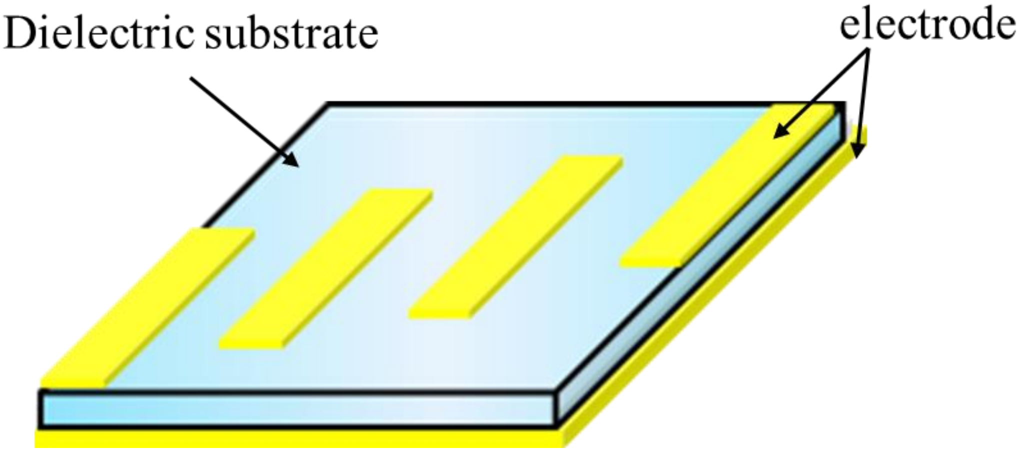

Figure 1-7 Schematic diagram of microstrip line-type filter device

1.6 Purpose and concept of this study

The purpose of this study is to investigate the dielectric properties of glass materials in the GHz-THz band in order to find promising substrate materials for 5G and 6G communications. To achieve this purpose, I established a method for measuring the complex permittivity of materials in the THz band. Then, I measured the complex permittivity of glass materials, particularly silicate glass, in the THz band, and analyzed the complex permittivity via molecular dynamic (MD) simulations to understand the origin of the complex permittivity in the 5G and 6G bands in silicate glass and to show the design concept for creating low-dielectric-loss glass materials. Moreover, I measured the temperature dependence of the dielectric constant and propose a glass-based material with a low temperature dependence of the dielectric constant. Finally, filter devices for the millimeter-wave band was fabricated to demonstrate their performance.

1.7 Flowchart of this study

In Chapter 2, I introduce our novel THz ellipsometer system as a method for measuring complex permittivity in the THz band. Other measurement methods are also described in this chapter. In Chapter 3, the effect of network modifiers in silicate glass on dielectric properties is investigated. I investigate examples of complex permittivity measurements of alkali silicate glasses are presented, along with the results of MD simulations, to explain the origin of the complex permittivity of alkali silicate glasses in the THz band. In addition, the guidelines for the fabrication of alkali silicate glasses that have low dielectric loss are also proposed. Moreover, I investigate the dielectric property of aluminoborosilicate glass with alkaline earth metal ions. In Chapter 4, the influence of network formers in sodium silicate glass on dielectric properties is investigated: I present the measurements and discuss the behavior of the complex permittivity of alkali silicate glasses containing Al or B. In Chapter 5, the temperature dependence results of the dielectric constant of glass materials is presented, and methods to reduce the temperature dependence of the dielectric constant are discussed. Furthermore, filter devices with low temperature dependence of dielectric constant were fabricated and the filter performance was measured. These results are also presented. In Chapter 6, I summarize the points clarified in this study.

Chapter 2

Development of Measurement System for Complex Permittivity in the GHz to THz Frequency Range

2.1 Introduction

Chapter 1 elucidated the importance of measuring the complex permittivity in the GHz to THz frequency range for establishing beyond 5G and sixth-generation (6G) communication systems. In this chapter, I present a method to establish a measurement system that can determine the complex permittivity in the GHz–THz frequency range.

2.2 Split-post dielectric resonator method

Split-post dielectric resonator (SPDR) method is a method to measure the accuracy of complex permittivity. The complex permittivity of samples at 10 GHz were determined using an SPDR developed by QWED (Figure 2-1), which was used to measure the Q-factors and resonance frequencies of the vacancy and samples.[58, 59] The 85071E (option 300) Materials Measurement Software package (Keysight Technologies) was used for the analysis. In the SPDR method, the dielectric constant of a sample in the range of 2–90 and loss tangent in the range of 0.00002–0.01 can be measured. Note that the actual frequency was marginally less than 10 GHz, depending on the thicknesses and dielectric constants of the samples; however, for simplicity, the complex permittivities were reported as the values measured at 10 GHz.

Figure 2-1 Photo of a Split-Post Dielectric Resonator (SPDR) system

2.3 Terahertz time-domain spectroscopy method

The THz-TDS method calculates the complex permittivity by comparing the amplitude and phase of a transmitted femtosecond pulse laser with and without the sample.[60, 61] The measurement range was approximately 0.5–5 THz, depending on the sample. TAS7400TS and TAS7400SU (Advantest) were used for the measurement (Figure 2-2). This method is based on the transmission through the sample, which indicates that the complex permittivity is determined based on the complex transmittance. As the transmittance of inorganic materials is significantly low, measurement samples were polished to a thickness of 100–200 μm before measurement. However, because multiple reflections occur inside a thin sample when measuring transmittance, this study used the following two methods to remove the effects of multiple reflections.

First, the transmission spectrum was checked, and areas that were clearly noisy were not used in the analysis. Second, the effects of multiple reflections were removed according to a previous study.[62] Two waveforms, that is, with and without the sample, $E_s(t)$ and $E_r(t)$, respectively, were measured and they are Fourier transformed into complex amplitudes as a function of the angular frequency, that is, $E_s(\omega)$ and $E_r(\omega)$, respectively. The ratio of $E_s(\omega)$ and $E_r(\omega)$ is formulated as follows:

$$\begin{gathered}\sqrt{T(\omega)}exp(-i\phi(\omega)) = \frac{\tilde{E}_s(\omega)}{\tilde{E}_r(\omega)} = \tilde{t}_{as}(\omega)\tilde{t}_{sa}(\omega)exp\left\{-i\frac{(\tilde{n}(\omega)-1)d\omega}{c}\right\} \times \\ \textstyle\sum_{l=0}^{m}\left\{(\tilde{r}_{sa}(\omega))^2 exp\left(-i\frac{\widetilde{2n}(\omega)d\omega}{c}\right)\right\},\end{gathered} \tag{2-1}$$

where $\tilde{n} = n - i\kappa$ and d are the complex refractive index and thickness of the sample, respectively, and $\tilde{t}_{as}$, $\tilde{t}_{sa}$, and $\tilde{r}_{sa}$ denote the complex Fresnel coefficients for amplitude transmission ($\tilde{t}$) and reflection ($\tilde{r}$) at the sample surfaces. The integer m represents the multiple reflections in the observation time domain. $T(\omega)$ and $\varphi(\omega)$ are the power transmittance and phase shift due to the sample. From the experimentally obtained $T(\omega)$ and $\varphi(\omega)$, I determined n and κ to be functions of frequency. However, n and κ cannot be expressed as explicit functions of $T(\omega)$ and $\varphi(\omega)$; therefore, Eq. (2-1) is modified as follows:

$$\begin{gathered}n(\omega) = \frac{c}{d\omega}\left\{\phi(\omega) + \frac{d\omega}{c} + arg[\tilde{t}_{as}(\omega)\tilde{t}_{sa}(\omega)] \times\right. \\ \left.\textstyle\sum_{l=0}^{m}\left\{(\tilde{r}_{sa}(\omega))^2 exp\left(-i\frac{\widetilde{2n}(\omega)d\omega}{c}\right)\right\}^{l}\right\},\end{gathered} \tag{2-2}$$

$$k(\omega) = -\frac{c}{2d\omega} \times \ln\frac{T(\omega)}{\left|\tilde{t}_{as}(\omega)\tilde{t}_{sa}(\omega)\sum_{l=0}^{m}\left\{(\tilde{r}_{sa}(\omega))^2 exp\left(-i\frac{\widetilde{2n}(\omega)d\omega}{c}\right)\right\}^{l}\right|}, \tag{2-3}$$

where l denotes the number of multiple reflections. In this study, the refractive index and extinction coefficient were calculated as $l = 3$.

THz-TDS is one of the few equipment that can measure dielectric properties in the THz band, but not all dielectric properties of glass materials can be measured at all wavelengths. When dielectric properties are obtained using THz-TDS, transmitted light from the sample is measured and calculated. This is because when calculating dielectric properties from reflection characteristics, the phase difference obtained by the sample setting method changes, and it is difficult to measure the exact phase difference caused by the sample. Since dielectric properties are obtained from transmittance measurements, it is difficult to obtain dielectric properties in a band where light does not transmit, and only the 0.5 to 3 THz band can be measured. In this study, when dielectric properties can be measured with THz-TDS, they were measured with THz-TDS. Also, there are errors in measurements with THz-TDS. One source of error is sample thickness. Glass with a thickness of about 100 μm was used in this study, and the thickness error at that time was about 2%, and the sample thickness deviation was about 5%. Since dielectric properties measured by THz-TDS have a proportional relationship with sample thickness, sample thickness errors directly become dielectric characteristic errors. Therefore, the total error in dielectric properties is found to be about 7%.

Figure 2-2 Photo of a terahertz time-domain spectroscopy system (TAS7400)

2.4 Far-infrared spectroscopic method

The far-infrared (FIR) spectroscopic method is used to calculate the complex permittivity from the measured transmittance and reflectance. This method is only applicable to samples with low dielectric loss. First, the transmittance is measured for two samples of different thicknesses. The internal transmittance is calculated by measuring the difference between the two transmittances, and the light absorption coefficient k of the sample is calculated as follows:

$$T = \exp\left(\frac{-4\pi kt}{\lambda}\right), \tag{2-4}$$

where T, t, and λ denote the transmittance, sample thickness, and wave number, respectively.

Furthermore, by measuring the infrared reflectance R, the refractive index n of the sample can be determined, as R is given by

$$R = \frac{(1-n)^2+k^2}{(1+n)^2+k^2}; \tag{2-5}$$

therefore,

$$n = \frac{-(1+R)+\sqrt{(1+R)^2-(1-R)(R-1+Rk^2-k^2)}}{R-1}. \tag{2-6}$$

Using these equations, n and k can be calculated, and the real and imaginary parts of the dielectric constant (ε', ε'', respectively) can be calculated as follows:

$$\varepsilon' = n^2 - k^2, \tag{2-7}$$

$$\varepsilon'' = 2nk. \tag{2-8}$$

2.5 Far-infrared spectroscopic ellipsometry

Spectroscopic ellipsometry is known as a measurement technique to obtain the optical constants of a sample by detecting polarized light that is reflected from a sample. In this research, the complex permittivity at 2–21 THz was determined using a FIR spectroscopic ellipsometer. This chapter reports on the performance of a uniquely constructed FIR spectroscopic ellipsometer and the analysis method.

Figures 2-3 and 2-4 show the photo and schematic diagram of Fourier-transform FIR (FT-FIR) spectroscopic ellipsometric system. The system was uniquely developed using an FT-FIR spectrometer (FARIS-1, JASCO, Japan). A Michelson interferometer in the Fourier-transform spectrometer is followed by a rotating-analyzer-type ellipsometer, which contains an additional compensator (C) in the optical path following a rotating wire-grid polarizer (P_R). Each part is housed in an aluminum chamber, and the internal part of the device can be evacuated using a rotary pump to prevent attenuation caused by water vapor and carbon dioxide in the air during measurement. The light source is a high-pressure mercury lamp, and the detector is a Si bolometer unit, which enables us to measure the FIR spectrum in the low-frequency region down to 0.75 THz (25 cm^{-1}). Three types of THz compensators (WP-CQ-L20-H20-OW61.5-L/4, WP-CQ-L20-H20-OW148-L/4, and WP-CQ-L20-H20-OW496-L/4, TYDEX, Russia) composed of crystal quartz were introduced separately between the polarizer and the sample for wideband spectral measurements. The measurable spectral range of the ellipsometric system was 0.75−21 THz (25−700 cm^{-1}). The position of the sample stage could be arbitrarily changed such that the light hits the center of sample surface at different incident angles. The reflected light was elliptically polarized owing to the difference in complex reflection coefficients between the p- and s-polarizations. The lights from the p- and s-polarized components were individually measured using a rotating wire-grid analyzer (A_R). The rotating polarizer, rotating analyzer, sample stage, and incident angle were controlled using stepping motor controllers (D250, Suruga Seiki, Japan) and a software was used to precisely measure the polarized state. Moreover, prior to the sample measurement, the residual calibration[63] was performed.

Here, I introduce the calculation of the two-layer model used in this experiment: when plane polarized light in medium(0) (usually vacuum) is incident on the sample medium(1), as shown in Figure 2-5, the complex amplitude reflectance values r_p and r_s and the ratio of incident light to reflected light are defined as follows for p-polarization parallel to the incident plane and s-polarization perpendicular to it, respectively.

$$r_p = \frac{N_1 \cos \phi_0 - N_0 \cos \phi_1}{N_1 \cos \phi_0 + N_0 \cos \phi_1} \tag{2-9}$$

$$r_s = \frac{N_0 \cos \phi_0 - N_1 \cos \phi_1}{N_0 \cos \phi_0 + N_1 \cos \phi_1} \tag{2-10}$$

Here, N_0 and N_1 are the complex refractive indices of the respective medium, φ_0 is an incident angle, and φ_1 is a refraction angle. The ratio of these two reflectance values is called the polarization ellipticity ρ and is expressed as follows:

$$\rho = \frac{r_p}{r_s}, \tag{2-11}$$

where r_p and r_s denote the reflectance values of the p- and s-polarized lights, respectively. Using the angle Ψ of the polarization plane of the reflected light and the change in the phase (ellipticity) of the polarization (Δ), ρ can also be expressed as follows:

$$\rho = \frac{r_p}{r_s} = \tan \psi \, exp(i\Delta), \tag{2-12}$$

$$\tan \psi = \frac{r_p}{r_s}, \tag{2-13}$$

$$\Delta = \Delta_p - \Delta_s. \tag{2-14}$$

The ellipsometer measures the ellipticity and phase of the reflected light, and the complex refractive index N_1 of the sample can be measured from Ψ and Δ.[64]

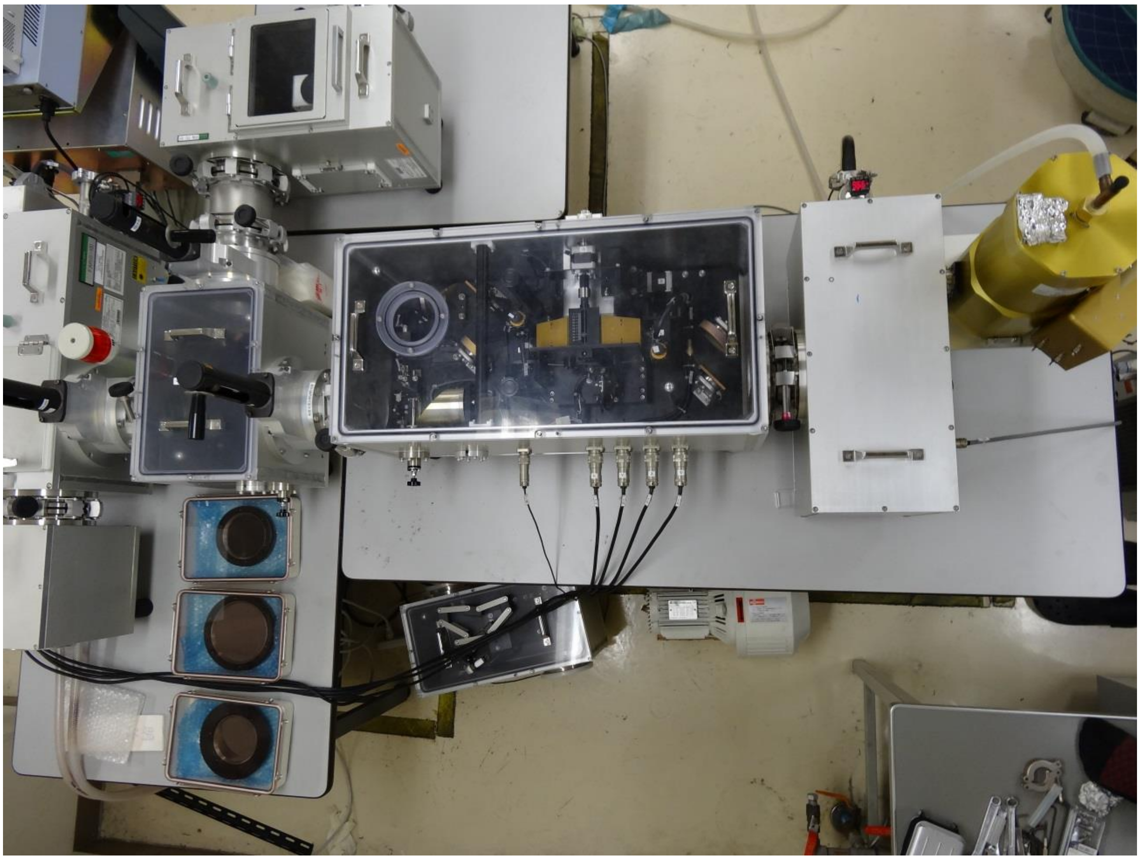

Figure 2-3 Photo of the Fourier-transform far-infrared (FT-FIR) spectroscopic ellipsometric system

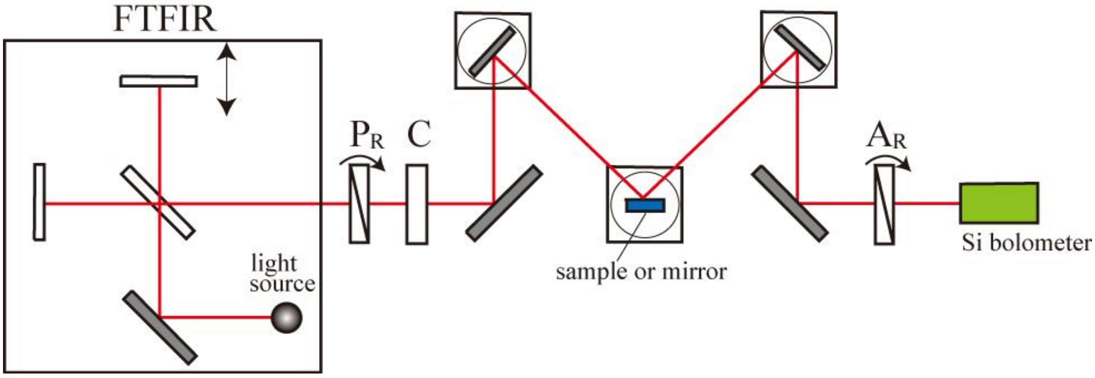

Figure 2-4 Schematic diagram of the FT-FIR spectroscopic ellipsometric system

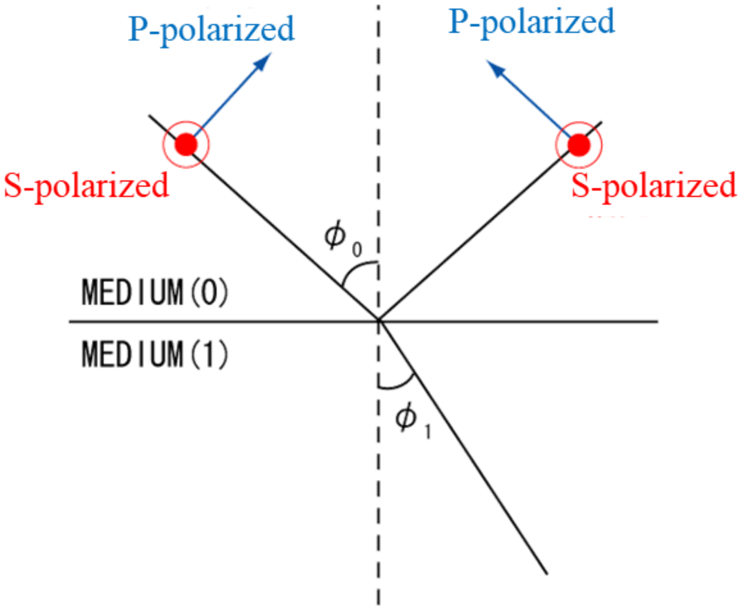

Figure 2-5 Schematic diagram of an optical two-layer model

2.6 Measurement method of the rotating-analyzer-type ellipsometer with compensator

Here, I explain the method used to calculate the complex permittivity from the measured intensity. For simplicity, I would like to discuss the case of a rotating-analyzer-type ellipsometer without a compensator. The Jones vector is usually used to analyze the change in polarization in a sample or optical element, and the relationship between the Stokes parameter and ellipsometric angles (ψ, Δ) can be obtained by calculating Jones matrix. The Jones matrix for a rotating-analyzer-type ellipsometer is obtained as follows:

$$\begin{bmatrix} E_{eout} \\ 0 \end{bmatrix} = \begin{bmatrix} 1 & 0 \\ 0 & 0 \end{bmatrix} \begin{bmatrix} \cos A & \sin A \\ -\sin A & \cos A \end{bmatrix} \begin{bmatrix} r_p & r_{ps} \\ r_{sp} & r_s \end{bmatrix} \begin{bmatrix} \cos P & -\sin P \\ \sin P & \cos P \end{bmatrix} \begin{bmatrix} 1 & 0 \\ 0 & 0 \end{bmatrix} \begin{bmatrix} 1 \\ 0 \end{bmatrix}, \tag{2-15}$$

where P is the angle of the polarizer, A is the angle of the detector, and Ψ and Δ are the optical constants of the sample as expressed in Eq. (2-15). If the sample is isotropic or has an accurate orientation, the off-diagonal terms r_{ps} and r_{sp} of the sample vector are zero; therefore, only the diagonal terms can be considered, and the following equations can be expressed by considering $\rho = r_p/r_s = \tan\varphi \exp(i\Delta)$.

$$I = |E_{eout}|^2 = EE^* \tag{2-16}$$

$$\begin{aligned} \mathrm{I} = I_0[(1 - cos2Pcos2\Psi) + (cos2P - cos2\Psi)cos2A \\ + (sin2Psin2\Psi cos\Delta)sin2A \end{aligned} \tag{2-17}$$

When the azimuth angle of the polarizer is set to 45° relative to the plane of reflection, the intensity I at the detector can be described in terms of Stokes parameters s_1, s_2, and s_0 as follows:[65]

$$I(A) = s_0 + s_1 \cos A + s_2\, sin\, 2\, A. \tag{2-18}$$

The Stokes parameters can be easily calculated from experimental results obtained under the analyzer setting of A = 0°, 45°, 90°, and 135° using the following equations:

$$s_0 = I(0) + I\left(\frac{\pi}{2}\right), \tag{2-19}$$

$$s_1 = I(0) - I\left(\frac{\pi}{2}\right), \tag{2-20}$$

$$s_2 = I(\pi/4) - I\left(\frac{3\pi}{4}\right). \tag{2-21}$$

Furthermore, the Stokes parameters are related to the ellipsometric parameters Ψ and Δ as follows:

$$s_1 = \frac{I_0 - I_{90}}{I_0 + I_{90}} = -\cos 2\psi, \tag{2-22}$$

$$s_2 = \frac{I_{45} - I_{135}}{I_0 + I_{90}} = \sin 2\psi \cos \Delta. \tag{2-23}$$

However, when Ψ takes a small value, as in the case of certain glass materials, the intensity of light becomes significantly small when the polarizer angle is 90°, resulting in a susceptibility to errors.

Therefore, the measurement accuracy can be improved by not shifting Ψ from 45°.

$$\varphi = \frac{1}{2} cos^{-1} \frac{\dfrac{I_{0^\circ} - I_{90^\circ}}{2I_m} - cos\,2P}{\dfrac{I_{0^\circ} - I_{90^\circ}}{2I_m} cos\,2P - 1} \tag{2-24}$$

$$\Delta = \cos^{-1} \frac{I_{45^\circ} - I_{135^\circ}}{2I_m} \frac{(1 - \cos 2\psi \cos 2P)}{\sin 2P \sin 2\psi} \tag{2-25}$$

By shifting the angle of P to 30° or 15°, highly accurate measurements can be obtained.

However, if Δ is close to 0° or 180°, a compensator or change in the incident angle is required to obtain accurate ellipsometric parameters. As an example, the Δ_0 and Ψ_0 of $SrTiO_3$ single crystal measured by our ellipsometer without compensator are shown in Figures 2-6 and 7. The ψ can be measured, but Δ is close to 180° and has a band where it cannot be measured. The experimental error of Ψ and Δ in the rotating-analyzer ellipsometry are proportional to (sin Δ)$^{-1}$;[66] thus, the experimental error in ellipsometric measurements of some materials is considerably large as the values of Δ for these materials are close to 0° or 180°. In such cases, the accuracy of measurements can be improved by incorporation of a compensator that shifts Δ in the rotating-analyzer-type ellipsometric system.[64] Therefore, three types of THz compensators were introduced separately between the polarizer and the sample for wideband spectral measurements.

The Jones matrix in a rotating analyzer-type ellipsometer with a rotating compensator is as follows

$$\begin{bmatrix} E_{eout} \\ 0 \end{bmatrix} = \begin{bmatrix} 1 & 0 \\ 0 & 0 \end{bmatrix} \begin{bmatrix} \cos A & \sin A \\ -\sin A & \cos A \end{bmatrix} \begin{bmatrix} \sin\varphi\, exp(i\Delta) & 0 \\ 0 & \cos\varphi \end{bmatrix} \begin{bmatrix} \cos C & -\sin C \\ \sin C & \cos C \end{bmatrix} \begin{bmatrix} exp(-i\delta) & 0 \\ 0 & 1 \end{bmatrix} \begin{bmatrix} \cos C & \sin C \\ -\sin C & \cos C \end{bmatrix} \begin{bmatrix} \cos P & -\sin P \\ \sin P & \cos P \end{bmatrix} \begin{bmatrix} 1 & 0 \\ 0 & 0 \end{bmatrix} \begin{bmatrix} 1 \\ 0 \end{bmatrix}, \qquad (2\text{-}26)$$

where δ is the phase difference created by the compensator. The Schematic diagram of the ellipsometric arrangement for measurements with a compensator is shown in Figure 2-8. The phase difference to be detected can be changed by the phase difference due to the compensator. By varying the angle of the compensator, it is possible to avoid the condition of Δ close to 0° or 180° for any value of Δ in the sample. However, these parameters contain mixed information related to the compensator and sample. For example, the values of Δ_1 and Ψ_1 of $SrTiO_3$ single crystal measured by our ellipsometer with compensator are shown in Figures 2-6 and 7. The phase difference certainly shifted to a lower angle; however, periodic noises were observed in the Δ_1 and Ψ_1 values. Because the thickness of the compensator was comparable to the wavelength of light, multiple reflections in the compensator occurred depending on the wavelength. This wavelength-dependent error is difficult to remove by only using calculations because the refractive index of the material of the compensator is also dependent on the wavelength. To remove the error caused by the compensator, The measurement was performed by measuring the light intensity multiple times at different angles of the compensator to cancel out multiple reflections. Specifically, it was calculated from the following equation

$$\varphi = \frac{1}{2} cos^{-1} \frac{\frac{\left(I_{90°,0°} - I_{90°,90°}\right) + \left(I_{0°,0°} - I_{0°,90°}\right)}{4I_m} - cos\,2P}{\frac{\left(I_{90°,0°} - I_{90°,90°}\right) + \left(I_{0°\_,0°} - I_{0°,90°}\right)}{4I_m} cos\,2P - 1} \tag{2-27}$$

$$\Delta = sin^{-1} - \sqrt{\frac{-(-\alpha^2 + \beta^2 - 1) - \sqrt{(-\alpha^2 + \beta^2 - 1)^2 - 4\alpha^2}}{2}} \tag{2-28}$$

$$\alpha = sin\Delta sin(\delta) = \frac{1 - \cos 2\psi \cos 2P}{sin\,2P\,sin\,2\psi} \frac{\left(I_{90°,45°} - I_{90°,\,135°}\right) - \left(I_{0°,45°} - I_{0°,\,135°}\right)}{4I_m} \tag{2-29}$$

$$\begin{aligned} \beta &= cos\Delta cos(\delta) \\ &= \frac{1 - \cos 2\psi \cos 2P}{sin\,2P\,sin\,2\psi} \frac{\left(I_{90°,45°} - I_{90°,\,135°}\right) + \left(I_{0°,45°} - I_{0°,\,135°}\right)}{4I_m} \end{aligned} \tag{2-30}$$

$$4I_m = I_{90°,0°} + I_{90°,\,90°} + I_{0°,0°} + I_{0°,\,90°} \tag{2-31}$$

The angle of the polarizer is *P*. The light intensity I_{CA} is described as *C* is the angle of the compensator and *A* is the angle of the detector. As an example, Δ_2 and Ψ_2 of $SrTiO_3$ single crystals are shown in Figures 2-6 and 7. Δ and Ψ of SrTiO3 were measured accurately.

The ellipsometer was used to determine the amplitude ratio of the polarized light ψ and phase difference Δ of the sample according as follows:[67]

$$\varepsilon' = \sin^2\theta_0 \left[1 + \frac{\tan^2\theta_0 \left(\cos^2 2\Psi - \sin^2 2\Psi \sin^2 \Delta\right)}{(1 + \sin 2\Psi \cos \Delta)^2}\right], \tag{2-32}$$

$$\varepsilon'' = \sin^2\theta_0 \frac{\tan^2\theta_0 \sin 4\Psi \sin \Delta}{(1 + \sin 2\Psi \cos \Delta)^2}, \tag{2-33}$$

where θ_0 is the incident angle of light.

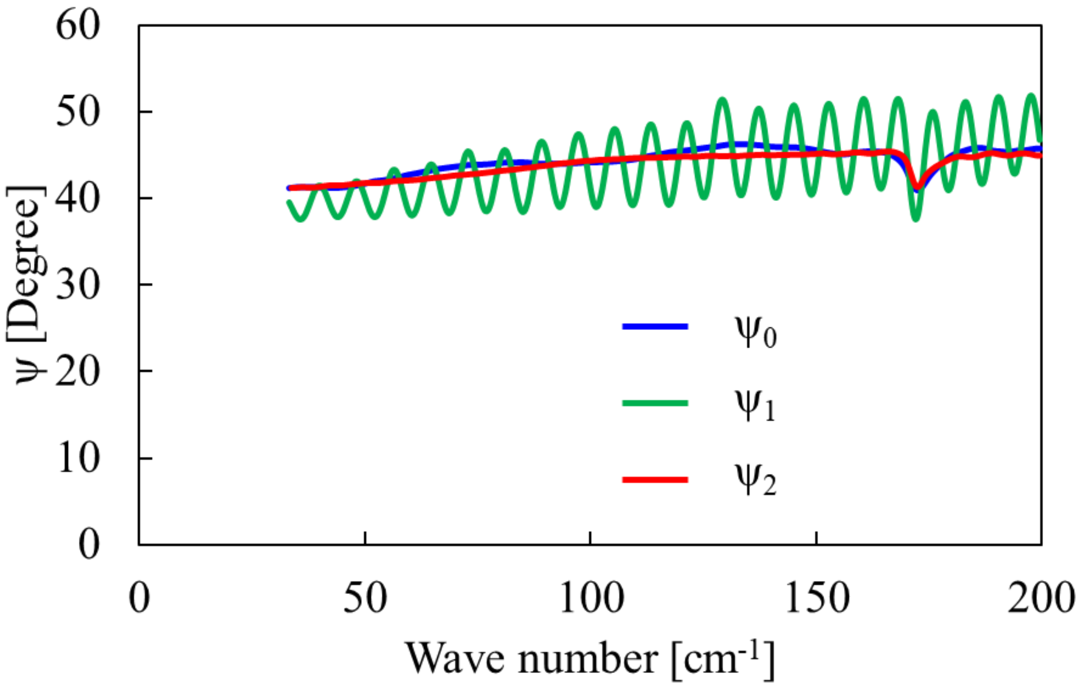

Figure 2-6 Ellipsometric parameters of $SrTiO_3$ single crystal. The Ψ_0 is the parameters measured without using a compensator. The Ψ_1 is measured with a compensator (WP-CQ-L20-H20-OW61.5-L/4) contain mixed information on the compensator and sample. The Ψ_2 is calibrated parameters of $SrTiO_3$ single crystal alone using three types of compensators.

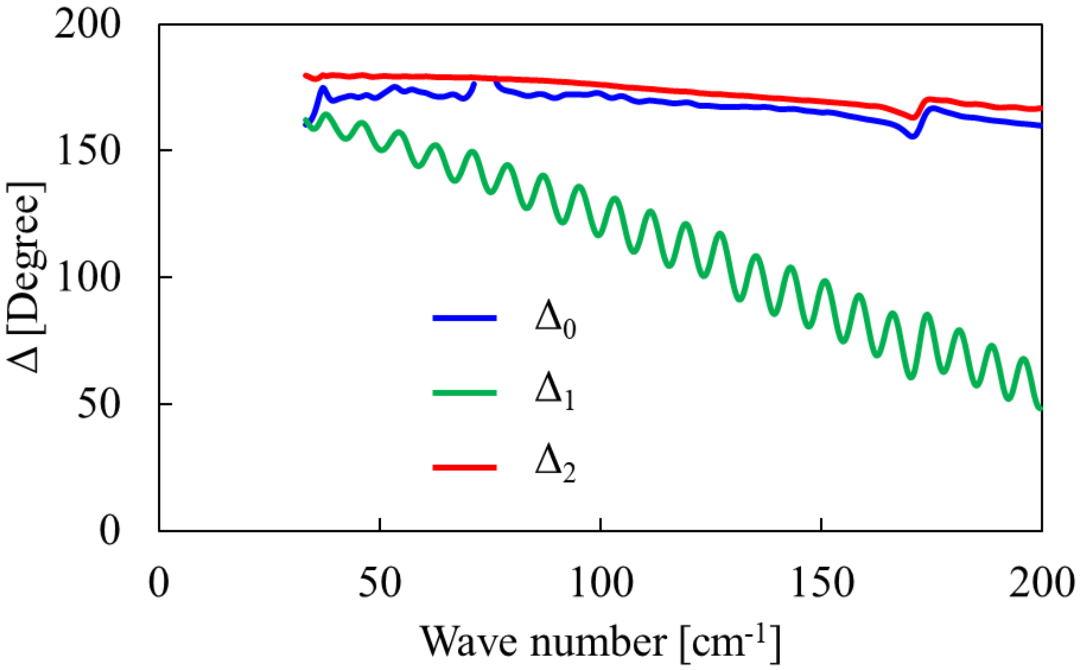

Figure 2-7 Ellipsometric parameters of $SrTiO_3$ single crystal. The Δ_0 is the parameters measured without using a compensator. The Δ_1 is measured with a compensator (WP-CQ-L20-H20-OW61.5-L/4) contain mixed information on the compensator and sample. The Δ_2 is calibrated parameters of $SrTiO_3$ single crystal alone using three types of compensators.

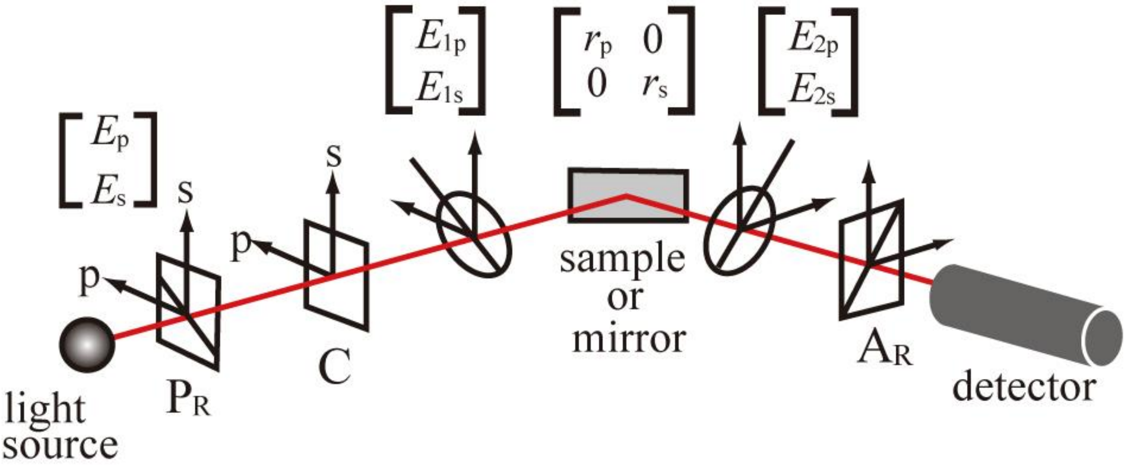

Figure 2-8 Schematic diagram of the ellipsometric arrangement for measurements with a compensator

2.7 Measurement of complex permittivity of $SrTiO_3$ single crystal using the developed spectroscopic ellipsometer

Using Eqs. (2-32) and (2-33), the complex permittivity of $SrTiO_3$ single crystal at 25−700 cm^{-1} (0.75−21 THz) was determined as shown in Figure 2-9.[68] The responses of the Slater, Last, and Axe modes, which are all optical phonon modes of $SrTiO_3$ at room temperature,[69, 70] were clearly observed. Notably, the dielectric dispersion of $SrTiO_3$ in the THz region is well described by the damped harmonic oscillator model:[69–72]

$$\varepsilon^*(\omega) = \varepsilon'(\omega) - i\varepsilon''(\omega) = \varepsilon_\infty \prod_{j=1}^{n} \frac{\omega_{j\mathrm{LO}}^2 - \omega^2 + i\gamma_{j\mathrm{LO}}\omega}{\omega_{j\mathrm{TO}}^2 - \omega^2 + i\gamma_{j\mathrm{TO}}\omega}, \tag{2-34}$$

where ε_∞ is the complex permittivity due to electric polarization, $\omega_{j\mathrm{LO}}$ and $\omega_{j\mathrm{TO}}$ are the resonance frequencies of the j-th longitudinal optical (LO) and transverse optical (TO) modes, respectively, and $\gamma_{j\mathrm{LO}}$ and $\gamma_{j\mathrm{TO}}$ are the damping factors of the LO and TO modes, respectively. As a fitting result using this model, the resonance frequencies of the Slater, Last, and Axe modes were estimated to be 91.9, 171.0, and 544.1 cm^{-1}, respectively. The relative permittivity in the low-frequency region was estimated as 302, which was almost consistent with the electrically measured value in the MHz region. As mentioned in previous reports,[69, 70] the Slater mode (or soft mode) governs the dielectric properties in the low-frequency region. The dotted lines in Figure 2-9 show the dielectric function reported by Kamarås *et al.*,[69] which has been estimated based on only unpolarized reflectance. The ellipsometric data are in agreement with the dielectric function that is estimated by unpolarized reflectance. Therefore, I conclude that a precise dielectric dispersion of $SrTiO_3$ single crystal at 25−700 cm^{-1} (0.75−21 THz) was directory measured using the developed FIR spectroscopic ellipsometer. Note that this measured value is not entirely accurate. Various factors have been considered for errors in measured values of dielectric properties with ellipsometers.[66] This equipment assumes that the polarizer angle, incidence angle, *etc.* have been adjusted, and only errors associated with changes in light intensity are described. The main possible errors in this measurement system are the polarization angle of the polarizer and the angle of incidence. If the polarization angle is off by 0.5 degrees and the incidence angle is off by 1 degree, the dielectric constant and dielectric loss are calculated to have an error of about 10%.

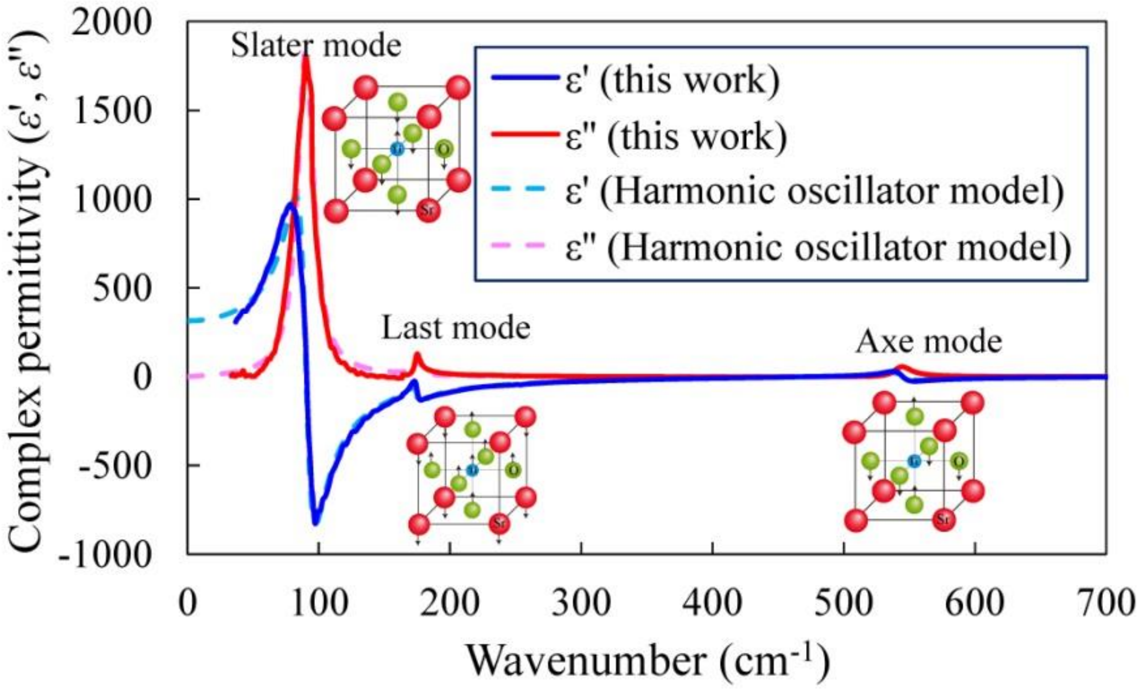

Figure 2-9 Complex permittivity of the $SrTiO_3$ single crystal in the THz region. The Slater, Last, and Axe mode responses are clearly observed at 92, 175, 545 cm^{-1}, respectively.

2.8 Measurement of complex permittivity of sodium silicate glass in GHz–THz frequencies

In Section 2.7, I showed that the complex permittivity of strontium titanate single crystals in GHz−THz frequencies can be measured by our developed ellipsometer. Next, we attempted to measure the complex permittivity of glass materials using THz-TDS and our ellipsometer. Figure 2-10 shows the complex permittivity of silica glass and $70SiO_2$-$30Na_2O$ glass. Solid and dotted lines represent values measured by terahertz ellipsometer and THz-TDS, respectively. Points indicate values estimated with the split post dielectric resonator technique. The split post dielectric resonator developed by QWED, which was used to measure the Q-factors and resonance frequencies of the vacancy and the samples.[58, 59] The 85071E (option 300) software package (Keysight Technologies) was used for the analysis. For both silica and soda-silicate glasses, the complex permittivities measured by THz-TDS and those obtained using our developed ellipsometer are almost continuously connected, and the validity of the measurements is high. The complex permittivity measurements at 10 GHz by the split post dielectric resonator method were found to be an extension of the THz-TDS measurements. Furthermore, the reflectance of $70SiO_2$-$30Na_2O$ glass calculated from the measured complex permittivity is shown in Figure 2-11. Kamitsos *et al.* measured the reflectance in a glass of the same composition and found it to be in close agreement with our calculations.[22] For these reasons, I conclude that this measurement system is also effective for measuring the complex permittivity of glass materials in GHz−THz frequencies. Assuming an error of 1° in the angle of incidence of light in the ellipsometer and an error of 0.5° in the polarizer, the error in the dielectric properties of $70SiO_2$-$30Na_2O$ glass is shown in Figure 2-12,13. The error in the angle of incidence leads to an error in the dielectric properties of about 10%, and the error in the polarizer leads to an error in the dielectric properties of a few percent.

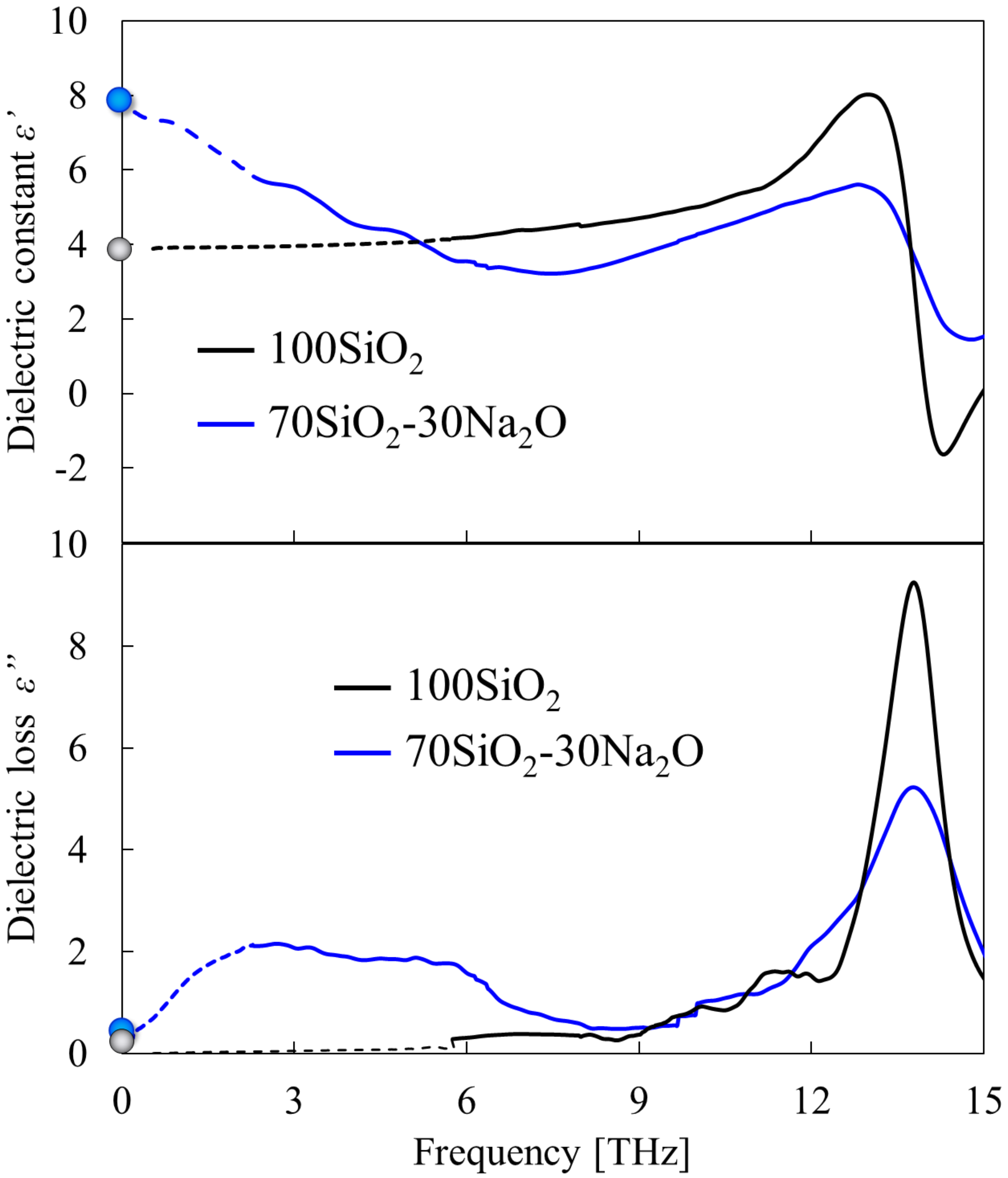

Figure 2-10 Frequency dependence of complex permittivity of silica glass and sodium silicate glasses. Solid and dotted lines represent values measured by terahertz ellipsometer and THz-TDS, respectively. Points indicate values estimated with the split post dielectric resonator technique.

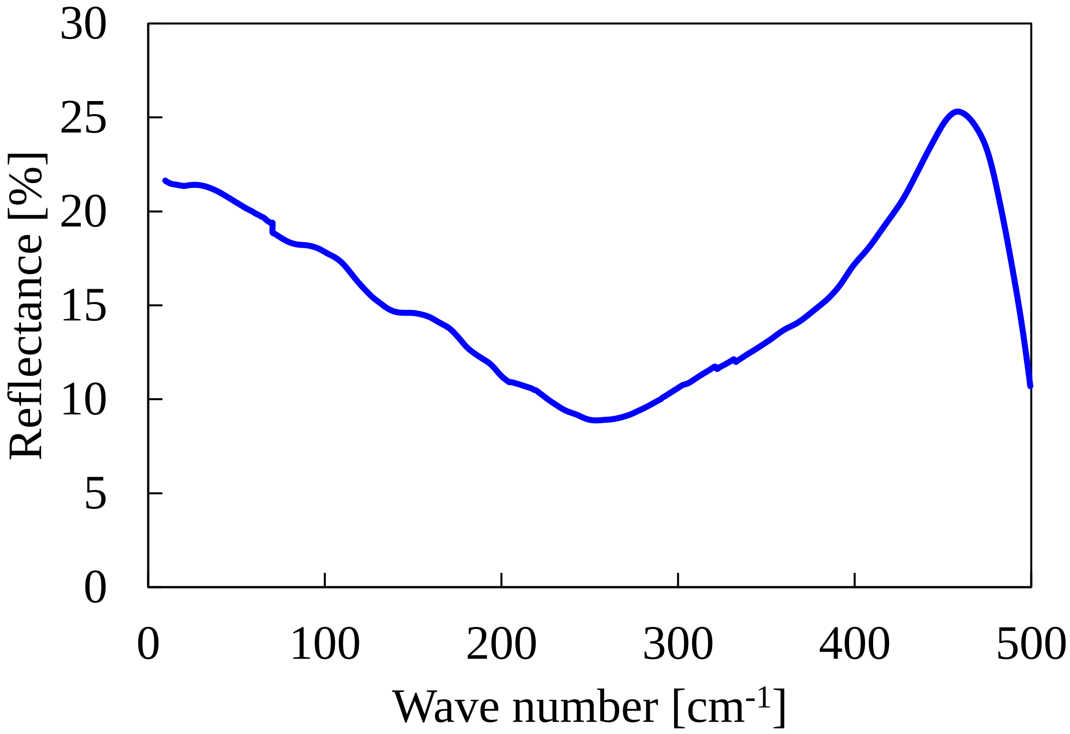

Figure 2-11 Reflectance of $70SiO_2$-$30Na_2O$ glass calculated from complex permittivity

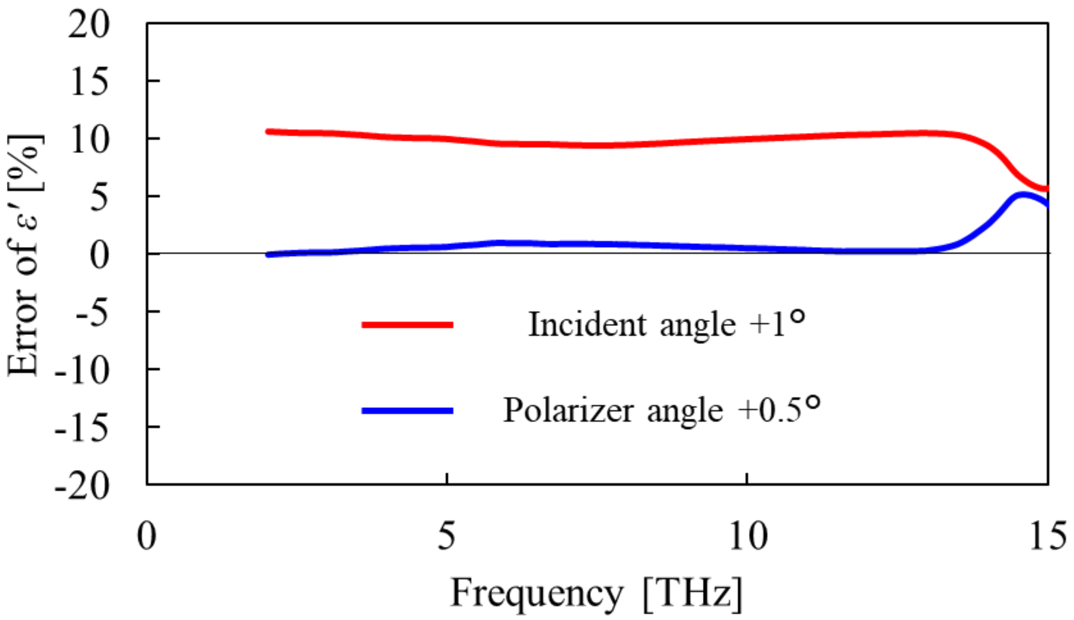

Figure 2-12 Error of dielectric constant in $70SiO_2$-$30Na_2O$ glass measured by terahertz ellipsometer.

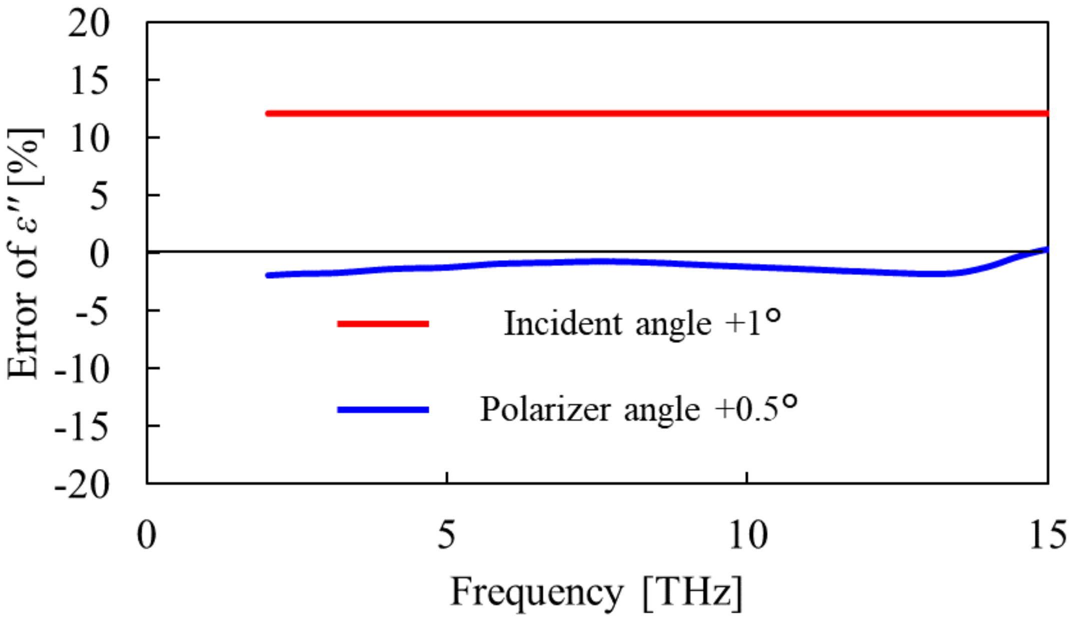

Figure 2-13 Error of dielectric loss in $70SiO_2$-$30Na_2O$ glass measured by terahertz ellipsometer.

2.9 Applicability of complex permittivity measurement method in the THz band

The previous chapters have introduced measurement methods using THz-TDS and ellipsometers, but there are cases where complex permittivity cannot be measured using these methods alone. THz-TDS measurements can only be applied at a maximum frequency of 7 THz due to the difficulty of constructing the optical system necessary for measurements in the high frequency band.[73] Since THz-TDS detects light transmitted through a sample, if the transmittance of the sample is too low, the complex permittivity cannot be measured. On the other hand, ellipsometer measures the polarized reflected light from the sample, which results in a large measurement error for samples with low reflectance. The range of complex permittivity that can be measured by our ellipsometer and the THz-TDS are estimated. The results are shown in Figure 2-14. The measurement frequency was assumed to be 3 THz, and the calculations were based on the assumption that reflectance of at least 15% is required for measurement by ellipsometer and transmittance of at least 15% is required for measurement by THz-TDS. Materials with high dielectric constant or dielectric loss have high reflectance and are easy to measure with an ellipsometer. Ellipsometry is a method for accurately measuring the complex permittivity of materials with high dielectric constant or dielectric loss. THz-TDS is a method for accurately measuring the complex permittivity of materials with low dielectric loss. However, the complex permittivity of materials with intermediate values of permittivity and dielectric loss is not accurate when measured with either measuring instrument. An example of a material with such properties is a resin material. Therefore, it is difficult to measure the complex permittivity of resin materials using our system, and this will be a measurement challenge for future understanding of complex permittivity in the THz band.

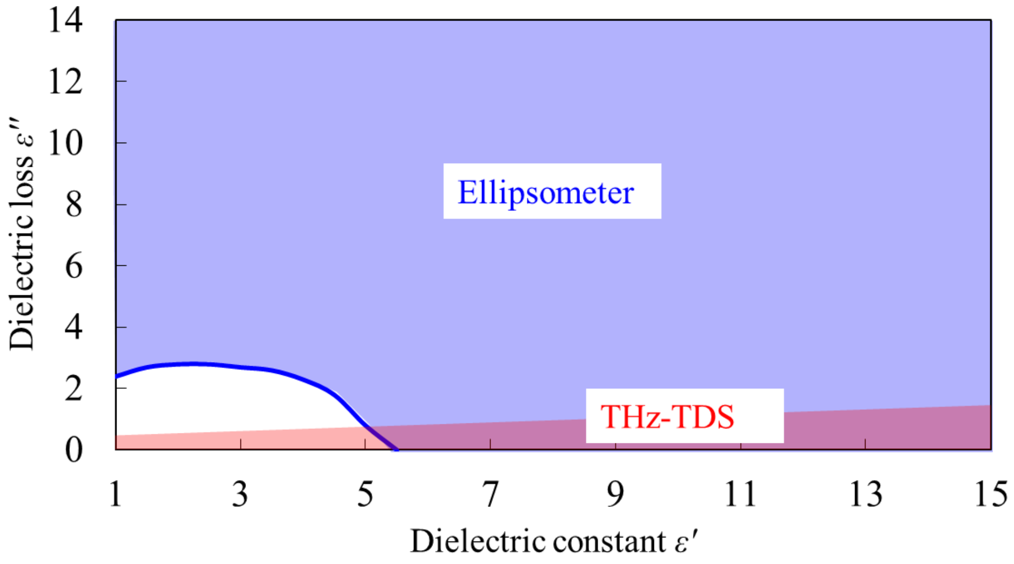

Figure 2-14 Complex permittivity measurement range by ellipsometer and THz-TDS.

2.10 Summary

To identify materials with good properties in the 5G and 6G bands, I investigated several methods for measuring the complex permittivity of materials in the GHz–THz bands. I used different methods to measure the complex permittivity. For example, methods using resonator and vector network analyzer, THz-TDS, and measurement of FIR transmittance, reflection of the sample, and ellipsometric technique were used. Among these methods, the FIR ellipsometer is an originally developed system. The complex permittivity of the $SrTiO_3$ single crystal as a standard sample was measured using the developed ellipsometer, and the ellipsometric data agreed with the dielectric function that was estimated using unpolarized reflectance data. The complex permittivity of glass samples was also shown to be measurable over a wide bandwidth when combined with THz-TDS. Therefore, the complex permittivity in the GHz–THz bands could be directly measured using our equipment. Thus, I believe that these methods are key techniques for understanding the dielectric properties of materials from a phononic perspective and can be powerful tools in the search for useful materials for application in 5G and 6G systems.

Chapter 3

Effect of Network Modifier on Dielectric Response of Silicate Glasses in GHz–THz Frequency Range

3.1 Introduction

In Chapter 2, a method for measuring dielectric properties in the GHz and THz bands was proposed and its investigative results were presented. Subsequently, the dielectric properties of glass materials, which are useful for 5G and 6G communication systems, were measured in the GHz–THz range using previous reported methods and the results are analyzed in this chapter. Moreover, MD calculations were used to understand the origin of dielectric properties in the glass materials.

Among oxide glasses, silicate glass is widely used because of its high chemical stability, whereas silica glass is difficult to produce owing to its high melting temperature. Therefore, silicate glasses often contain alkali metal or alkali metal earth ions, which is network modifier, to reduce the melting temperature and improve productivity. For example, alkali aluminosilicate glasses that are used to cover mobile devices contain multiple alkali metal ions, such as Li, Na, and K ions, and the soda-lime silicate glasses used for windows often contain Na and K and Ca ions.[74–77]

Therefore, in this study, I investigated the effect of network modifiers on the dielectric properties of silicate glass aimed to measure the dielectric properties of single-alkali silicate glasses and to discuss their polarization mechanisms. To identify the effects of network modifier ions on the dielectric properties, I examined seven types of alkali silicate glasses: $70SiO_2$-$30Na_2O$, $60SiO_2$-$40Na_2O$, $80SiO_2$-$20Na_2O$, $70SiO_2$-$30Li_2O$, $70SiO_2$-$30K_2O$, $70SiO_2$-$30Rb_2O$, $70SiO_2$-$30Cs_2O$ and four types of mixed-alkali silicate glasses: $70SiO_2$-$15Li_2O$-$15Na_2O$, $70SiO_2$-$15Li_2O$-$15K_2O$, $70SiO_2$-$15Na_2O$-$15K_2O$, $70SiO_2$-$10Li_2O$-$10Na_2O$-$10K_2O$ and three types of alminoborosilicateglass with alkali metal earth ion: $50SiO_2$-$10Al_2O_3$-$20B_2O_3$-$20CaO$, $55SiO_2$-$10Al_2O_3$-$20B_2O_3$-$15CaO$, $60SiO_2$-$10Al_2O_3$-$20B_2O_3$-$10CaO$. Furthermore, I measured the dielectric responses up to the THz range to evaluate the dielectric properties at GHz bands and to understand how the GHz dielectric properties of the glasses were affected by the dielectric responses in the THz range.[78]

3.2 Experimental Procedure

The sodium silicate glass samples containing 20-40 mol% sodium oxide (80SiO_2-20Na_2O, 70SiO_2-30Na_2O, 60SiO_2-40Na_2O) and alkali-silicate glass samples containing 30 mol% alkali-metal oxides (70SiO_2-30Li_2O, 70SiO_2-30Na_2O, 70SiO_2-30K_2O, 70SiO_2-30Cs_2O, and 70SiO_2-30Rb_2O) and mixed-alkali-silicate glass samples containing 30 mol% alkali-metal oxides (70SiO_2-15Li_2O-15Na_2O, 70SiO_2-15Li_2O-15K_2O, 70SiO_2-15Na_2O-15K_2O, 70SiO_2-10Li_2O-10Na_2O-10K_2O) and alminoborosilicate glass samples (50SiO_2-10Al_2O_3-20B_2O_3-20CaO, 55SiO_2-10Al_2O_3-20B_2O_3-15CaO, 60SiO_2-10Al_2O_3-20B_2O_3-10CaO) were prepared using a conventional melting method. The glasses were melted in 500 g batches of pure-silica sand and alkali carbonates. First, the batch materials were melted in a platinum crucible at 1400–1650 °C for 2 h. Then, the melted glasses were quenched by pouring them into cold water, which broke them into small pieces. The resulting glass cullet was dried for approximately 24 h at 80 °C to remove water and then re-melted in a platinum crucible at 1400–1650 °C for 2 h to obtain homogeneous bubble-free melted glasses. The molten glasses were poured into steel formworks preheated at 200 °C, held at the glass transition temperatures (490–650 °C) for 1 h, and then cooled to room temperature (~25 °C) at a rate of 1 °C/min to reduce thermal stress. The glass transition temperature of each glass was estimated from references.[79–81] The resulting glasses were cut and polished to produce 35 × 35 × 0.5 mm sheet samples for the dielectric measurements. The two widest surfaces were mirror-polished with CeO_2 powder. Silica glass purchased from Crystal Base Corporation was used for comparison. After polishing, the glass samples were stored in a box with silica gel to prevent the absorption of moisture from the atmosphere.

The dielectric properties of the glasses in the gigahertz frequency range were evaluated using three different techniques. First, the complex permittivities of the samples at 10 GHz were determined using the split post dielectric resonator developed by QWED, which was used to measure the Q-factors and resonance frequencies of the vacancy and the samples.[58, 59] The 85071E (option 300) software package (Keysight Technologies) was used for the analysis. Note, the actual frequency was slightly less than 10 GHz, depending on the thicknesses and dielectric constants of the samples; however, for simplicity, the complex permittivities are reported as the values measured at 10 GHz.

Second, the complex permittivities of the samples at 0.5–2 THz were determined using THz-TDS (TAS7400TS and TAS7400SU, ADVANTEST). The results were calculated by comparing the amplitude and phase of a transmitted femtosecond pulse laser with and without the sample.[60, 82] This method is based on the transmission of the sample, which indicates that the complex permittivity is determined by the complex transmittance.

Third, the complex permittivity at 2–10 THz was determined using an FIR ellipsometer system,[83] which was developed based on a Fourier transform FIR spectrometer (FARIS1, JASCO).

3.3 Molecular Dynamics Simulations

MD simulations were performed using the LAMMPS software package[84] to calculate the dielectric functions of the glasses at GHz–THz frequencies. The glass models were prepared using the general melt quench method.[85] Partial charge pair potentials with parameters proposed by Teter and later extended by Du *et al.* were used.[86] A cut off distance of short-range interaction is 12 Å. The time step for integrating atom motions was 1 fs. The polarizations induced by the AC electric field were determined by following the method proposed in ref 39. Glass models composed of approximately 5000 atoms were obtained using the melt-quenching method. The atoms were initially placed in a random reticular pattern at 2.7 Å intervals. The models were held at 3500 K for 500 ps and then monotonically cooled to 500 K at 1 K/ps under isobaric conditions (0.1 MPa) using an isothermal–isobaric (NPT) ensemble.[88] The cooled glass model was then held at 500 K for 500 ps (time required to ensure sufficient equilibration). The final length of the cubic MD cells after thermal equilibration was approximately 48.6 Å.

The MD simulations were then switched from the NPT ensemble to a canonical (NVT) ensemble. Before applying the electric field, a slab model was prepared with a vacuum layer approximately 100 Å thick in the *z*-direction. The slab model was held at 500 K for 300 ps to relax the atomic positions near the boundary. An AC electric field $E(t) = E_0 \sin(2\pi ft)$ was applied in the *z*-direction, where E_0 and f are the magnitude and frequency of the electric field, respectively. In this study, E_0 was set to 0.1 V/Å and f was varied from 10 GHz to 10 THz. The polarization P in the *z*-direction was calculated using the following equation:

$$P(t) = \sum_{i=1}^{N} \frac{eq_i}{V} r_i(t), \tag{3-1}$$

where e is the elementary charge, q_i is the effective charge of the i-th atom, V is the volume of the glass part, r_i is the displacement of the i-th atom in the z-direction, and N is the number of atoms. Note, P and r_i are time dependent under an AC electric field. The effective charge was set to 60% of the ionic charge of each ion.[86] To determine the loss tangent tanδ, P(t) was fitted using the following equations:

$$P_0 = \frac{1}{4}\int_0^{1/f} |P(t)| \mathrm{d}t, \tag{3-2}$$

and

$$P(t) = P_0 \sin{(2\pi f t + \delta)}. \tag{3-3}$$

The resulting value of δ was used to calculate the complex permittivity (ε', ε'') according to the following equations:

$$\varepsilon' = 1 + \frac{P_0}{E_0 \varepsilon_0} \cos\delta, \tag{3-4}$$

and

$$\varepsilon'' = \frac{P_0}{E_0 \varepsilon_0} \sin\delta, \tag{3-5}$$

where ε_0 is the permittivity of a vacuum.

3.4 Result and Discussion

This section is not available in the outline version.

3.5 Summary

In this chapter, the dielectric properties of pure silica and alkali silicate glasses were investigated at 0.5–10 THz using THz-TDS and FIR spectroscopic ellipsometry. Silica glass exhibited significantly minimal dielectric dispersion (0.5–10 THz, with a low dielectric constant and loss). In contrast, alkali silicate glasses exhibited high dielectric dispersion, and the dielectric constant and loss were higher than those of silica glass. This dispersion affects the dielectric properties in the GHz band. The calculated MD data were in good agreement with the experimental data. The results suggest that alkali metal ions vibrate and migrate owing to the applied electric field, which affects the dielectric constant and loss in the GHz–THz frequency range. To obtain glasses with low dielectric loss in the GHz band, it is important to minimize the content of alkali metal ions with low atomic numbers. The inclusion of multiple alkali metal ions in the glass suppresses the frequency of migration of alkali metal ions, resulting in lower dielectric loss in the GHz band. On the other hand, alkaline earth metal ions also affect dielectric properties in the same way as alkali metal ions.

Chapter 4

Effect of Network Former on Dielectric Response of Sodium Silicate Glasses in GHz–THz Frequency Range

4.1 Introduction

In Chapter 3, the dielectric dispersion in alkali silicate glasses was revealed to be larger when containing more alkali ions, with a narrower and larger dispersion for heavier alkali elements. The results of the MD analysis also suggest that the dielectric dispersion in alkali silicate glasses is determined by the vibration and exchange of alkali ions. Similarly, the effect of alkaline earth metal elements on the dielectric properties of the glass was also found: the greater the amount of alkaline earth metal, the greater the dielectric constant and dielectric loss, and it is estimated that the dielectric properties are affected by the vibration of the alkaline earth metal elements,

However, there are two main types of glass-constituting elements: network formers, which form the framework of the glass, and network modifiers, which break down the framework of the glass. In the previous chapter, the effect of network modifiers on the dielectric properties of silicate glass was investigated. The elements that change the properties of glass include network modifiers, which break the glass network, as well as network formers, which build the glass network. Alkali and alkaline earth ions are typical network modifiers, whereas Al and B ions are typical network formers. For example, Al ions are known to improve the strength in alkali aluminosilicate glasses that are used as cover glass[76]. Borosilicate glass is also widely used as a scientific and chemical product because the thermal expansion coefficient can be controlled by including B in the glass component.[112] Thus, the properties of glasses used in different applications are controlled by using components other than silica as network-forming oxides. The dielectric response of different alkali ion as network modifiers in glass was presented in the previous chapter, and in this chapter, the effect of network formers on the dielectric properties of silicate glass was investigated.

4.2 Experimental procedure

The alkali aluminosilicate and alkali borosilicate glass samples containing 30 mol% alkali metal oxides ($60SiO_2$-$10Al_2O_3$-$30Na_2O$, $50SiO_2$-$20Al_2O_3$-$30Na_2O$, $60SiO_2$-$10B_2O_3$-$30Na_2O$, $50SiO_2$-$20B_2O_3$-$30Na_2O$, and $40SiO_2$-$30B_2O_3$-$30Na_2O$) were prepared using a conventional melting method. The glasses were melted in 500 g batches comprising pure-silica sand, alumina sand, boron oxide, and sodium carbonates. First, the batch materials were melted in a platinum crucible at 1400–1700 °C for 2 h. Then, the melted glasses were quenched by pouring them into cold water, which broke them into small pieces. The resulting glass cullet was dried for approximately 24 h at 80 °C to remove water and then re-melted in a platinum crucible at 1400–1700 °C for 2 h to obtain homogeneous bubble-free melted glass. The molten glass was poured into steel formworks that were preheated at 200 °C, which were maintained at the glass transition temperatures for 1 h and then cooled to room temperature (~25 °C) at a rate of 1 °C/min to reduce thermal stress. The resulting glasses were cut and polished to produce 35 mm × 35 mm × 0.1–0.7 mm sheet samples for the dielectric measurements. The two widest surfaces were mirror-polished with CeO_2 powder. After polishing, the glass samples were stored in a box with silica gel to prevent the absorption of moisture from the atmosphere.

The dielectric properties of the glass samples in the GHz frequency range were evaluated using three different techniques. First, the complex permittivities of the samples at 10 GHz were determined using a SPDR that was developed by QWED, which was used to measure the Q-factors and resonance frequencies of the vacancy and samples.[58, 59] The 85071E (option 300) software package (Keysight Technologies) was used for the analysis. Notably, the actual frequency was marginally less than 10 GHz, depending on the thicknesses and dielectric constants of the samples; however, for simplicity, the complex permittivities are reported as the values measured at 10 GHz.

Second, the complex permittivities of the samples at 0.5–2 THz were determined using THz-TDS (TAS7400TS and TAS7400SU, ADVANTEST). The results were calculated by comparing the amplitude and phase of a transmitted femtosecond pulse laser with and without the sample.[60, 82] This method is based on the transmission of the sample, which indicates that the complex permittivity is determined by the complex transmittance.

Third, the complex permittivity at 2–10 THz was determined using an FIR spectroscopic ellipsometer system and spectroscopic method,[83] which was developed based on a FT-FIR spectrometer (FARIS1, JASCO). This ellipsometer was a rotating-analyzer-type device with a compensator that measured the polarization of the light reflected off the sample surface.

4.3 Results and discussion

This section is not available in the outline version.

4.4 Summary

In this chapter, I investigated the dielectric properties of sodium silicate glass with Al and B, which function as network formers in glass. When Al ions were included in the network former, the dielectric constant and dielectric loss of the glass at 10 GHz increased. On the other hand, when B ions were included in the network former, the dielectric constant and dielectric loss of the glass at 10 GHz were almost unchanged. To understand the reason for this, we measured the complex permittivity in the THz band. As a result, we confirmed the effect that the peak value of dielectric loss becomes higher when Al or B ions are included as a glass network. On the other hand, the peak frequency of dielectric loss shifted to the lower wavenumber side when Al ions entered the glass, whereas it shifted to the higher wavenumber side when B ions entered the glass. This difference is thought to affect the GHz dielectric properties of the glass.

Chapter 5

Fabrication of and Evaluation Prototype Filter Device Using Glass-Ceramic Material

5.1 Introduction

In addition to low insertion loss, filter devices require another characteristic for their effective functioning, that is, the low temperature dependence of the operating frequency of the filter.[117–119] The frequency that can be used for communication is determined by the standards developed in each country, and the operating frequency of the filter device must not change with temperature. In general, because the operating frequency of filter devices is determined based on the resonance of the electric field, materials that do not alter the resonance frequency are required. For example, in SAW filters, a filter device called temperature-compensated SAW was developed, which suppresses the temperature variation of the resonance frequency by using a quartz substrate.[117–119] Because glass and LTCC materials are used in MSL-type filters, the temperature dependence of the resonance frequency is expressed by τ_f, which is determined using the following equation.[120]

$$\tau_f = -\frac{\tau_\alpha}{2} - \alpha \tag{5-1}$$

Here, τ_α denotes the temperature dependence of the dielectric constant and α is the thermal expansion coefficient.[121] The thermal expansion coefficient of glass materials is generally only a few ppm/K[122, 123]; however, the temperature coefficient of the dielectric constant is approximately 100 ppm/K.[5, 124] Therefore, the temperature-dependent rate of change of the dielectric constant must be reduced when developing filter devices. One method to reduce the temperature dependence of the dielectric constant is to combine glass materials with materials that have a negative temperature dependence of the dielectric constant, and various such materials are known.[125–129] For example, in an MSL filter made with LTCC, by adding ST, the τ_f is 20 ppm/k.[121] In this study, I considered rutile, which is a material that is compatible with glass. Rutile is used as a nucleating material in the preparation of crystallized glass (i.e., a material in which crystals precipitate homogeneously in glass).[74, 130–133] Rutile has no dipole moment and has a negative temperature dependence of dielectric constant over a wide frequency range from GHz to sub-THz.[125] Furthermore, rutile is known to have a sufficiently low dielectric loss in the GHz band[134], and its low dielectric loss properties are not compromised when reduced in glass. In this study, I attempted to fabricate a material with low dielectric loss and temperature dependence of dielectric constant by adding TiO_2 to the composition of glass and heat-treating it to reduce rutile. Filter devices operating in the millimeter-wave band were fabricated using the obtained materials, and their performance as filters was measured.

5.2 Experimental procedure

Aluminoborosilicate glass samples containing SiO_2, Al_2O_3, B_2O_3, and minimum required alkaline earth metal elements with 0, 3, 5, and 7 mol% TiO_2 were prepared using a conventional melting method. The glass samples were melted in 1 kg batches of pure-silica sand and other oxides and carbonates. First, the batch materials were melted in a platinum crucible at 1400–1600 °C for 2 h. Then, the melted glass samples were quenched by pouring them into cold water, which broke them into small pieces. The resulting glass cullet was dried for approximately 24 h at 80 °C to remove water and then re-melted in a platinum crucible at 1400–1600 °C for 2 h to obtain homogeneous bubble-free molten glass samples. The molten glass samples were poured into steel formworks that were preheated at 200 °C, and then maintained at the glass transition temperature (730 °C) for 1 h, followed by cooling to room temperature (~25 °C) at a rate of 1 °C/min to reduce thermal stress. A portion of the resulting glass was heat-treated at 900°C for 4 h to obtain crystallized glass. The resulting glasses were cut and polished to produce 35 mm × 35 mm × 0.3 mm sheet samples for the dielectric measurements. The two widest surfaces were mirror-polished with CeO_2 powder. The heat-treated glass was ground and mixed with 10 wt% ZnO as a standard material, and its X-ray diffraction (XRD) patterns were measured. The resulting diffraction data were analyzed via the Rietveld method using the RIETAN-FP analysis program.[135] The surface roughness Ra after crystallization was measured using a laser microscope (Keyence VK-200).

The dielectric properties of the glass samples in the GHz frequency range were evaluated using the cavity resonator method. A cavity resonator manufactured by Kanto Electronic Applications was used for the measurement. The cavity resonator method determines the complex permittivity by measuring the resonance frequency and Q value when a sample is inserted inside the resonator or cavity. The measurements were obtained in accordance with the Japanese Industrial Standards JIS R 1641 using a vector network analyzer (E8361C, Keysight). Note that the actual frequency was marginally less than 28 GHz, depending on the thicknesses and dielectric constants of the samples; however, for simplicity, the complex permittivities are reported as the values measured at 28 GHz. The temperature dependence of the dielectric constant was also measured using the cavity resonator method. The resonator and wiring were placed in a thermostatic chamber (Espec SH-241) for blank and sample measurements. A total of five temperatures were measured: −20, 0, 25, 40, and 60 °C. Note that the actual frequency was marginally less than 35 GHz, depending on the thicknesses and dielectric constants of the samples; however, for simplicity, the complex permittivities are reported as the values measured at 35 GHz. Finally, a filter device was designed using the material with the smallest temperature dependence of the dielectric constant. The center frequency was set to 28 GHz, and a Chebyshev bandpass filter with five resonator stages was designed to balance the skirt characteristics and insertion loss.[4] Filter devices were fabricated by drawing the designs onto a substrate using lithographic techniques and copper plating. The characteristics of the resulting devices were measured using the vector network analyzer and a microprobe. Measurement temperatures were −20, 0, 25, and 40 °C.

5.3 Results and discussion

This section is not available in the outline version.

5.4 Summary

To establish communication systems in the high-frequency band, filter devices adapted to the high-frequency band are important. However, conventional filter devices such as SAW and bulk acoustic wave filters are not applicable to frequency bands above the millimeter wave. Therefore, MSL filters using glass or glass-ceramic materials have attracted attention. Because glass has a low dielectric loss and high quality flatness, low-loss filters can be fabricated. In this chapter, filter devices fabricated using glass-ceramic substrates are described. The temperature dependence of the dielectric constant was reduced by rutile crystals in the glass. The filter device was operated in the millimeter-wave band and exhibited a significantly low temperature dependence and low insertion loss. This technology can be applied for beyond 5G and 6G bands.

Chapter 6

General Conclusion

In this thesis, I have investigated the dielectric properties of glass materials at the GHz–THz band, which are important for beyond 5G and 6G communication systems.

In Chapter 1, the various properties required for beyond 5G and 6G materials are surveyed. Flatness and dielectric property are important; thus, this result indicates that glass materials are potential candidates for high-frequency communications. However, the dielectric properties of glass materials in the high-frequency band have not yet been clearly understood, which is a problem when using the glass materials.

In Chapter 2, I proposed a method for measuring dielectric properties in the high-frequency band. The measurement of dielectric properties in the GHz–THz band, especially in the high-frequency band above 1 THz, has been difficult using commercially available equipment. Thus, in this study, a THz ellipsometer was developed to measure the complex permittivity in the THz band. As the accurate measurement of the dielectric properties of materials with large Δ is difficult using THz ellipsometers, compensators were introduced to measure a variety of materials in the THz band. As a reference material, the complex permittivity of $SrTiO_3$ single crystal was measured using the developed ellipsometer system and the results showed good agreement with the complex permittivity predicted from harmonic oscillator model analysis. Our developed ellipsometer system demonstrated its effectiveness for measuring complex permittivity in the THz band. Furthermore, the dielectric properties of glass materials in the THz band were measured using a combination of THz-TDS and a THz ellipsometer. Calculation of reflectance from the obtained dielectric properties showed good agreement with previous literature values, indicating that dielectric properties in the THz band can be measured with the appropriate combination of instruments.

The dielectric properties of silicate glass, the most commonly used glass material in industry, in the high-frequency band were investigated and the results were analyzed in Chapter 3. In particular, the effect of network modifier on the dielectric properties was investigated, which revealed that the component of alkali metal ions in alkali silicate glasses causes a broad dielectric relaxation in the 1–9 THz band, and the dielectric relaxation in this band significantly affects the dielectric properties in the GHz band. To understand the origin of the dielectric relaxation in this band, I analyzed the movement of the ions via MD simulations, which revealed that the dielectric relaxation was caused by the vibration and migration of alkali metal ions. When the number of electrons of the alkali metal ions is less, the influence of these alkali metal ions is less, and even a small amount of alkali metal ions can reduce the dielectric relaxation and produce glass with low dielectric loss. It was also shown that the mixed-alkali effect can be used to further reduce the complex permittivity in the GHz band. Furthermore, the effect of Ca ions in aluminoboro silicate glass on dielectric properties was investigated. As a result, it became clear that the effect of alkaline earth metal elements on the dielectric properties of glass is the same as that of alkali metal ions, i.e., they increase the dielectric constant and dielectric loss. This result indicates that alkaline earth metal elements and alkali metal elements have similar effects, and it is desirable to add optimal amounts of each element while maintaining a balance between viscosity and dielectric properties.

In Chapter 4, the effect of network modifier on the dielectric properties was investigated. When network former ions such as Al ion was substituted for Si in sodium silicate glass, the dielectric constant and dielectric loss at 10 GHz increased. Contrary, when network former ions such as B ion was substituted for Si in sodium silicate glass, the dielectric constant and dielectric loss at 10GHz remained unchanged. The difference in dielectric properties between the two is presumably due to the addition of Al and B ions to soda silicate glass, which changes the state of Na ions in the glass. Therefore, to obtain a glass material with low dielectric loss in the GHz band, silica and boron ion must be used as the network former.

In Chapter 5, the low temperature dependence of dielectric constant was investigated, which is a property required by filter devices for beyond 5G and 6G communications. Because the temperature coefficient of the dielectric constant of glass is positive, I was able to reduce the temperature dependence of the dielectric constant by homogeneously depositing rutile crystals, which have a negative temperature dependence of dielectric constant, into the glass. Furthermore, filter devices were fabricated using the obtained glass-ceramic substrates and their performance was demonstrated. The fabricated glass-ceramic filter device demonstrated a low insertion loss and no temperature dependence.

In conclusion, this paper discussed the dielectric properties of glass materials, which are promising materials for beyond 5G and 6G systems, in the GHz–THz band. I measured the dielectric property of glass materials in the GHz–THz band using the developed THz ellipsometer system. The dielectric properties of glass in the beyond 5G and 6G bands were revealed to be strongly influenced by the dielectric properties in the THz band. The dielectric properties of glass materials are determined by the vibration and migration of network modifiers, such as alkali metal ions and alkaline earth metal ions in the glass. To control the vibration and migration of the network modifier in the glass, the mixed-alkali effect is useful and Al should not be incorporated instead of Si as network formers for dielectric property. The filter device was demonstrated. The temperature dependence of the dielectric constant, which is important factor for filter device can be controlled by depositing rutile crystals in the glass. Finally, filter devices were fabricated, and filter device characteristics with low insertion loss and low temperature dependence were obtained. This achievement will be important for the utilization of the glass materials in the high-frequency band in the future.

Publication lists

- **K. Kanehara**, S. Urata, S. Yasuhara, T. Tsurumi, T. Hoshina, “Dielectric response and polarization mechanism of alkali silicate glasses in gigahertz to terahertz frequency range”, *J. Am. Ceram. Soc.*, 106, 5341–5350 (2023).
- **K. Kanehara**, S. Urata, S. Yasuhara, T. Tsurumi, T. Hoshina, “Dielectric property and polarization mechanism of sodium silicate glass in GHz–THz range”, *Jpn. J. Appl. Phys.*, 61, SN1001 (2022).
- **K. Kanehara**, T. Hoshina, H. Takeda, T. Tsurumi, “Terahertz permittivity of rutile TiO_2 single crystal measured by anisotropic far-infrared ellipsometry”, *J. Ceram. Soc. Jpn.*, 123, 303-306 (2015).
- **K. Kanehara**, T. Hoshina, H. Takeda, T. Tsurumi, “Measurement of ionic polarization of $SrTiO_3$ single crystal by far-infrared spectroscopic ellipsometry”, *Appl. Phys. Lett.*, 105, 042901 (2014).

Acknowledgment

Throughout the course of my graduate research, I owe a great debt of gratitude to several people who provided me several kinds of assistances.

I would like to show me grateful appreciation my advisor Associate Professor Takuya Hoshina for his guidance and support. Since the day I joined research group, he has always given me pithy and important advice for overcoming difficulties. Emeritus Professor Takaaki Tsurumi taught me how to think not only about academics but also about life. Assistant Professor Sou Yasuhara, as a person close to my age, showed me the importance of taking a doctoral program. I am deeply grateful to them. And I thank the members of my thesis committee, Professor Tetsuji Yano, Professor Akira Nakajima, Professor Nobuhiro Matsushita, Associate Professor Tetsuo Kishi, for providing helpful comment on the thesis. I appreciate the kind support form Ms. Satomi Ii.

In addition, I appreciate the help of Dr. Shingo Urata, Mr. Kazuhiko Niwano, Mr. Nobutaka Kidera, Dr. Akio Koike, Dr. Shigeki Sawamura, Dr. Seiki Ohara, and Dr. Satoshi Yoshida. I thank to AGC Inc. colleagues.

I also thank all members in the laboratory. I really enjoyed my life in Tokyo Tech.

Finally, I wish to express my sincere gratitude to my family. My parents have always loved me and encourage me to become a scientist. My beloved wife Mei has always helped me to execute this study.

March 2024

Kazuki Kanehara

References

1. Zhang L, Liang YC, Niyato D. 6G Visions: Mobile ultra-broadband, super internet-of-things, and artificial intelligence. *China Commun*. 2019;16(8):1–14. https://doi.org/10.23919/JCC.2019.08.001
2. Giordani M, Zorzi M. Satellite Communication at Millimeter Waves: A Key Enabler of the 6G Era. *2020 Int. Conf. Comput. Netw. Commun. ICNC 2020*. Institute of Electrical and Electronics Engineers Inc.; 2020:383–388. https://doi.org/10.1109/ICNC47757.2020.9049651
3. Huang B, Jia Q. Accurate Modeling of Conductor Rough Surfaces in Waveguide Devices. *Electron 2019, Vol 8, Page 269*. 2019;8(3):269. https://doi.org/10.3390/ELECTRONICS8030269
4. Hong J-S. Microstrip filters for RF/microwave applications. 2011;635.
5. Dernovsek O, Naeini A, Preu G, Wersing W, Eberstein M, Schiller WA. LTCC glass-ceramic composites for microwave application. *J Eur Ceram Soc*. 2001;21(10–11):1693–1697. https://doi.org/10.1016/S0955-2219(01)00096-6
6. Zhou J. Towards rational design of low-temperature co-fired ceramic (LTCC) materials. *J Adv Ceram*. n.d.;2012(2):89–99. https://doi.org/10.1007/s40145-012-0011-3
7. Cai L, Wu J, Lamberson L, *et al.* Glass for 5G applications. *Appl Phys Lett*. 2021;119(8):082901. https://doi.org/10.1063/5.0057324
8. Lanagan MT, Cai L, Lamberson LA, Wu J, Streltsova E, Smith NJ. Dielectric polarizability of alkali and alkaline-earth modified silicate glasses at microwave frequency. *Appl Phys Lett*. 2020;116(22):222902. https://doi.org/10.1063/5.0008646
9. Ali M, Watanabe A, Lin TH, Tentzeris M, Tummala R, Raj PM. Ultra-wideband, glass package-integrated power dividers for 5G and MM-wave applications. *2019 IEEE Int. Symp. Antennas Propag. Usn. Radio Sci. Meet. APSURSI 2019 - Proc.* Institute of Electrical and Electronics Engineers Inc.; 2019:863–864. https://doi.org/10.1109/APUSNCURSINRSM.2019.8888980
10. Watanabe AO, Ali M, Zhang R, *et al.* Glass-Based IC-Embedded Antenna-Integrated Packages for 28-GHz High-Speed Data Communications. *Proc. - Electron. Components Technol. Conf.* Vols. 2020-June. Institute of Electrical and Electronics Engineers Inc.; 2020:89–94. https://doi.org/10.1109/ECTC32862.2020.00027
11. Sakudo T. Solid State Physics －Lattics Dynamics and Dielectric Phase Transitions－. 6th ed. Tokyo: Shokabo; 1993
12. Cai L, Shi Y, Hrdina K, *et al.* Low-temperature vibrational dynamics of fused silica and binary silicate glasses. *Phys Rev B*. 2018;97(5):1–6. https://doi.org/10.1103/PhysRevB.97.054311
13. Lunkenheimer P, Loidl A. Response of disordered matter to electromagnetic fields. *Phys Rev Lett*. 2003;91(20):20–23. https://doi.org/10.1103/PhysRevLett.91.207601
14. Hoshina T. Size effect of barium titanate: Fine particles and ceramics. *J Ceram Soc Japan*.

2013;121(1410):156–161. https://doi.org/10.2109/jcersj2.121.156

15. Hoshina T, Takizawa K, Li J, Kasama T, Kakemoto H, Tsurumi T. Domain size effect on dielectric properties of barium titanate ceramics. *Jpn J Appl Phys*. 2008;47(9 PART 2):7607–7611. https://doi.org/10.1143/JJAP.47.7607
16. Bilzer C, Devolder T, Crozat P, Chappert C, Cardoso S, Freitas PP. Vector network analyzer ferromagnetic resonance of thin films on coplanar waveguides: Comparison of different evaluation methods. *J Appl Phys*. 2007;101(7):74505. https://doi.org/10.1063/1.2716995/918841
17. Venkatesh MS, Raghavan GS V. An overview of dielectric properties measuring techniques. *Can Biosyst Eng*. 2005;47:15.
18. Sakamaki R, Horibe M, Yoshida M, Tsurumi T. Demonstration of dielectric measurement using a probe-backside reflection method up to 300 GHz. *Jpn J Appl Phys*. 2019;58(SLLE02):1–7. https://doi.org/10.7567/1347-4065/ab36f6
19. Kamarás K, Barth KL, Keilmann F, *et al.* The low-temperature infrared optical functions of SrTiO3 determined by reflectance spectroscopy and spectroscopic ellipsometry. *J Appl Phys*. 1998;78(2):1235. https://doi.org/10.1063/1.360364
20. Ponomareva I, Bellaiche L, Ostapchuk T, Hlinka J, Petzelt J. Terahertz dielectric response of cubic BaTi O3. *Phys Rev B - Condens Matter Mater Phys*. 2008;77(1):012102. https://doi.org/10.1103/PHYSREVB.77.012102/FIGURES/3/MEDIUM
21. Kamitsos EI, Chryssikos GD. Alkali sites in glass. *Solid State Ionics*. 1998;105(1–4):75–85. https://doi.org/10.1016/S0167-2738(97)00451-7
22. J.A.Kapoutsis, E. I. Kamitsos, G. D. Chryssikos, Y>D. Yiannopoulos, A. P. Patsts MP. Alkali sites in silicate glasses. *Proceefings Int Symp Glas Sci Technol*. 1994;23:341–346.
23. M.D. Ingram, J.E. Davidson, A.M. Coats, E.I. Kamitsos and JAK. Origins of anomalous mixed-cation effects in ion-exchanged glasses.pdf. *Glas Ber Glas Sci Technol*. 2000;73:89–104.
24. Krishnaswami S, Jain H, Kamitsos EI, Kapoutsis JA. Connection between the microwave and far infrared conductivity of oxide glasses. *J Non Cryst Solids*. 2000;274(1–3):307–312. https://doi.org/10.1016/S0022-3093(00)00193-9
25. Kamitsos EI. Infrared studies of borate glasses. *Phys Chem Glas*. 2003;44(2):79–87.
26. Kamitsos EI, Karakassides MA, Chryssikos GD. Cation - network interactions in binary alkali metal borate glasses. A far-infrared study. *J Phys Chem*. 1987;91(22):5807–5813. https://doi.org/10.1021/j100306a058
27. Yiannopoulos YD, Chryssikos GD, Kamitsos EI. Structure and properties of alkaline earth borate glasses. *Phys Chem Glas*. 2001;42(3):164–172.
28. Kamitsos EI, Chryssikos GD, Karakassides A. Investigation of the Cation-Site Interactions. 1987;(15):1067–1073.
29. Kamitsos EI, Karakassides MA, Chryssikos GD. Vibrational spectra of magnesium-sodium-

borate glasses. 2. Raman and mid-infrared investigation of the network structure. *J Phys Chem*. 1987;91(5):1073–1079. https://doi.org/10.1021/j100289a014

30. Kamitsos EI, Risen WM. Vibrational spectra of single and mixed alkali pentasilicate glasses. *J Non Cryst Solids*. 1984;65(2–3):333–354. https://doi.org/10.1016/0022-3093(84)90057-7

31. Dussauze M, Rodriguez V, Velli L, Varsamis CPE, Kamitsos EI. Polarization mechanisms and structural rearrangements in thermally poled sodium-alumino phosphate glasses. *J Appl Phys*. 2010;107(4). https://doi.org/10.1063/1.3305318

32. Devautour S, Varsamis CPE, Henn F, Kamitsos EI, Giuntini JC, Vanderschueren J. Dielectric relaxation and far-infrared spectroscopic study of cation-site interactions in oxide glasses. *J Phys Chem B*. 2001;105(24):5657–5662. https://doi.org/10.1021/jp004438x

33. Zhong J, Mori T, Fujii Y, *et al.* Molecular vibration and Boson peak analysis of glucose polymers and ester via terahertz spectroscopy. *Carbohydr Polym*. 2020;232:115789. https://doi.org/10.1016/J.CARBPOL.2019.115789

34. Terao W, Mori T, Fujii Y, Koreeda A, Kabeya M, Kojima S. Boson peak dynamics of natural polymer starch investigated by terahertz time-domain spectroscopy and low-frequency Raman scattering. 2017. https://doi.org/10.1016/j.saa.2017.11.051

35. Shibata ⇑ T, Mori T, Kojima S. Low-frequency vibrational properties of crystalline and glassy indomethacin probed by terahertz time-domain spectroscopy and low-frequency Raman scattering. 2015. https://doi.org/10.1016/j.saa.2015.05.059

36. Mori T, Masubuchi M, Fujii Y, *et al.* Boson Peak Investigation of Unusually Disproportionated Amorphous Silicon Monoxide via Terahertz Spectroscopy. *Int Conf Infrared, Millimeter, Terahertz Waves, IRMMW-THz*. 2020;2020-November:55–56. https://doi.org/10.1109/IRMMW-THZ46771.2020.9370985

37. Casella L, Baggioli M, Mori T, Zaccone A. Physics of phonon-polaritons in amorphous materials. *J Chem Phys*. 2021;154(1). https://doi.org/10.1063/5.0033371

38. Kojima S, Matsuda Y, Kodama M, Kawaji H, Atake T. Boson peaks and excess heat capacity of lithium borate glasses. *Chinese J Phys*. 2011;49(1):414–419.

39. Kojima S, Matsuda Y, Fukawa Y, *et al.* Boson peaks of lithium borate glasses studied by inelastic neutron and light scattering. 2010. https://doi.org/10.1016/j.jnoncrysol.2010.03.042

40. Chumakov AI, Monaco G, Fontana A, *et al.* Role of disorder in the thermodynamics and atomic dynamics of glasses. *Phys Rev Lett*. 2014;112(2):025502. https://doi.org/10.1103/PHYSREVLETT.112.025502/FIGURES/4/MEDIUM

41. Kojima S. Low-frequency Raman investigation of the liquid-glass transition in glycerol. *Phys Rev B*. 1993;47(5):2924–2927. https://doi.org/10.1103/PhysRevB.47.2924

42. Baggioli M, Zaccone A, Pérez-Castañeda T, *et al.* Boson peaks of glassy mono-and polyalcohols studied by inelastic neutron scattering. *J Phys Condens Matter*. 2000;12:5143–5154.

43. Duan Y, Fujii Y, Hijiya H, *et al.* Boson peak behavior of sodosilicate glasses probed by terahertz time-domain spectroscopy. *APS*. 2021;2021:M71.165.

44. Cai L, Wu J, Lamberson L, *et al.* Glass for 5G applications. *Appl Phys Lett*. 2021;119(8). https://doi.org/10.1063/5.0057324

45. Lanagan MT, Cai L, Lamberson LA, Wu J, Streltsova E, Smith NJ. Dielectric polarizability of alkali and alkaline-earth modified silicate glasses at microwave frequency. *Appl Phys Lett*. 2020;116(22):222902. https://doi.org/10.1063/5.0008646

46. Shannon RD. Dielectric polarizabilities of ions in oxides and fluorides. *J Appl Phys*. 1993;73(1):348–366. https://doi.org/10.1063/1.353856

47. Stevels JM. LOCAL MOTIONS IN VITREOUS SYSTEMS. *J NonCrystalline Solids*. 1980;40:69–82.

48. Jain H, Krishnaswami S, Kanert O. “Jellyfish” fluctuations of atoms in solids. *J. Non. Cryst. Solids*. Vols. 307–310. 2002:1017–1023. https://doi.org/10.1016/S0022-3093(02)01567-3

49. Kajita S. Function of RF modules and sensors in the IoT world. *J Japan Inst Electron Packag*. 2018;21(5):380–385. https://doi.org/10.5104/jiep.21.380

50. Wada T, Ogami T, Horita A, *et al.* A new tunable SAW filter circuit for reconfigurable RF. *IEEE MTT-S Int. Microw. Symp. Dig.* Vols. 2016-Augus. Institute of Electrical and Electronics Engineers Inc.; 2016 https://doi.org/10.1109/MWSYM.2016.7540110

51. Chen P, Li G, Zhu Z. Development and Application of SAW Filter. *Micromachines*. 2022;13(5):656. https://doi.org/10.3390/mi13050656

52. Krishnaswamy S V., Rosenbaum J, Horwitz S, Vale C, Moore RA. Film bulk acoustic wave resonator technology. *Ultrason. Symp. Proc.* Vol. 1. Publ by IEEE; 1990:529–536. https://doi.org/10.1109/ULTSYM.1990.171421

53. Zhang Y, Luo J, Flewitt AJ, Cai Z, Zhao X. Film bulk acoustic resonators (FBARs) as biosensors: A review. *Biosens Bioelectron*. 2018;116:1–15. https://doi.org/10.1016/J.BIOS.2018.05.028

54. Aigner R. Saw and bastechnologies for rf filter applications: a review ofthe relative strengths and weaknesses. *Proc. - IEEE Ultrason. Symp.* 2008:582–589. https://doi.org/10.1109/ULTSYM.2008.0140

55. Morgan D, Paige EGS. Surface acoustic wave filters: With applications to electronic communications and signal processing. 2007

56. Shirakawa AA, Pham JM, Jarry P, Kerhervé E. Design of FBAR filters at high frequency bands. *Int J RF Microw Comput Eng*. 2007;17(1):115–122. https://doi.org/10.1002/MMCE.20206

57. Yusuf Y, Cheng H, Gong X. Co-designed substrate-integrated waveguide filters with patch antennas. *IET Microwaves, Antennas Propag*. 2013;7(7):493–501. https://doi.org/10.1049/IET-MAP.2012.0431

58. Krupka J. Measurements of the complex permittivity of microwave circuit board substrates using

split dielectric resonator and reentrant cavity techniques. *Meas. complex permittivity Microw. circuit board substrates using Split Dielectr. Reson. reentrant cavity Tech.* Institution of Engineering and Technology (IET); 1996:21–24. https://doi.org/10.1049/CP:19960982

59. Krupka J, Gregory AP, Rochard OC, Clarke RN, Riddle B, Baker-Jarvis J. Uncertainty of complex permittivity measurements by split-post dielectric resonator technique. *J Eur Ceram Soc*. 2001;21(15):2673–2676. https://doi.org/10.1016/S0955-2219(01)00343-0

60. Nahata A, Weling AS, Heinz TF. A wideband coherent terahertz spectroscopy system using optical rectification and electro-optic sampling ARTICLES YOU MAY BE INTERESTED IN. *Cite as Appl Phys Lett*. 1996;69:2321. https://doi.org/10.1063/1.117511

61. Duvillaret L, Garet F, Coutaz JL. A reliable method for extraction of material parameters in terahertz time-domain spectroscopy. *IEEE J Sel Top Quantum Electron*. 1996;2(3):739–745. https://doi.org/10.1109/2944.571775

62. Hangyo M, Nagashima T, Nashima S. Spectroscopy by pulsed terahertz radiation. *Meas Sci Technol*. 2002;13(11):1727–1738. https://doi.org/10.1088/0957-0233/13/11/309

63. Collins RW. Automatic rotating element ellipsometers: Calibration, operation, and real-time applications. *Rev Sci Instrum*. 1990;61(8):2029. https://doi.org/10.1063/1.1141417

64. Ellipsometry S, Fujiwara AH. Spectroscopic Ellipsometry: Principles and Applications. John Wiley and Sons; 2007 https://doi.org/10.1002/9780470060193

65. Röseler A. IR spectroscopic ellipsometry: instrumentation and results. *Thin Solid Films*. 1993;234(1–2):307–313. https://doi.org/10.1016/0040-6090(93)90275-T

66. Nijs JMM de, Silfhout A van. Systematic and random errors in rotating-analyzer ellipsometry. *JOSA A, Vol 5, Issue 6, pp 773-781*. 1988;5(6):773–781. https://doi.org/10.1364/JOSAA.5.000773

67. Azzam RMA, Bashara NM. Ellipsometry and polarized light. Paperback ed. Amsterdam ;;New York: North-Holland ;Sole distributors for the USA and Canada Elsevier Science Pub. Co.; 1987

68. Kanehara K, Hoshina T, Takeda H, Tsurumi T. Measurement of ionic polarization of SrTiO3 single crystal by far-infrared spectroscopic ellipsometry. *Appl Phys Lett*. 2014;105(4). https://doi.org/10.1063/1.4891767

69. Kamarás K, Barth KL, Keilmann F, *et al.* The low-temperature infrared optical functions of SrTiO3 determined by reflectance spectroscopy and spectroscopic ellipsometry. *J Appl Phys*. 1998;78(2):1235. https://doi.org/10.1063/1.360364

70. Tsurumi T, Teranishi T, Wada S, *et al.* Ultra wide range dielectric spectroscopy of strontium titanate-strontium zirconate solid solution. *J Ceram Soc Japan*. 2006;114(1333):774–781. https://doi.org/10.2109/jcersj.114.774

71. Tsurumi T, Li J, Hoshina T, Kakemoto H, Nakada M, Akedo J. Ultrawide range dielectric spectroscopy of BaTiO3-based perovskite dielectrics. *Appl Phys Lett*. 2007;91(18):182905.

https://doi.org/10.1063/1.2804570

72. Hlinka J, Petzelt J, Kamba S, Noujni D, Ostapchuk T. Infrared dielectric response of relaxor ferroelectrics. *https://doi.org/101080/01411590500476438*. 2007;79(1–2):41–78. https://doi.org/10.1080/01411590500476438

73. Neu J, Schmuttenmaer CA. Tutorial: An introduction to terahertz time domain spectroscopy (THz-TDS). *J Appl Phys*. 2018;124(23):231101. https://doi.org/10.1063/1.5047659/13481510/231101_1_ACCEPTED_MANUSCRIPT.PDF

74. Axinte E. Glasses as engineering materials: A review. *Mater Des*. 2011;32(4):1717–1732. https://doi.org/10.1016/J.MATDES.2010.11.057

75. Hand RJ, Tadjiev DR. Mechanical properties of silicate glasses as a function of composition. *J Non Cryst Solids*. 2010;356(44–49):2417–2423. https://doi.org/10.1016/J.JNONCRYSOL.2010.05.007

76. Varshneya AK. Chemical Strengthening of Glass: Lessons Learned and Yet To Be Learned. *Int J Appl Glas Sci*. 2010;1(2):131–142. https://doi.org/10.1111/J.2041-1294.2010.00010.X

77. Sglavo VM. Chemical Strengthening of Soda Lime Silicate Float Glass: Effect of Small Differences in the KNO3 Bath. *Int J Appl Glas Sci*. 2015;6(1):72–82. https://doi.org/10.1111/IJAG.12101

78. Kanehara K, Urata S, Yasuhara S, Tsurumi T, Hoshina T. Dielectric property and polarization mechanism of sodium silicate glass in GHz–THz range. *Jpn J Appl Phys*. 2022;61(SN):SN1001. https://doi.org/10.35848/1347-4065/AC7B0F

79. Heslin MR, Shelby JE. Formation and properties of lithium neodymium silicate glasses. *J Non Cryst Solids*. 1994;167(1–2):172–179. https://doi.org/10.1016/0022-3093(94)90381-6

80. Wilkinson CJ, Potter AR, Welch RS, *et al.* Topological Origins of the Mixed Alkali Effect in Glass. *J Phys Chem B*. 2019;123(34):7482–7489. https://doi.org/10.1021/acs.jpcb.9b06512

81. O.v. mazurin, M.v. streltsina T p. shvaiko-shvaikovskaya, editor. Physical Sciences Data. 1983:II. https://doi.org/10.1016/b978-0-444-42215-6.50001-7

82. Duvillaret L, Garet F, Coutaz JL. A reliable method for extraction of material parameters in terahertz time-domain spectroscopy. *IEEE J Sel Top Quantum Electron*. 1996;2(3):739–745. https://doi.org/10.1109/2944.571775

83. Kanehara K, Hoshina T, Takeda H, Tsurumi T. Measurement of ionic polarization of SrTiO3 single crystal by far-infrared spectroscopic ellipsometry. *Appl Phys Lett*. 2014;105(4):042901. https://doi.org/10.1063/1.4891767

84. Plimpton S. Fast Parallel Algorithms for Short-Range Molecular Dynamics. *J Comput Phys*. 1995;117(1):1–19. https://doi.org/10.1006/JCPH.1995.1039

85. Urata S, Sato Y. A study on the plasticity of soda-lime silica glass via molecular dynamics simulations. *J Chem Phys*. 2017;147(17):174501. https://doi.org/10.1063/1.4997293

86. Du J, Cormack AN. The medium range structure of sodium silicate glasses: a molecular dynamics simulation. *J Non Cryst Solids*. 2004;349(1–3):66–79. https://doi.org/10.1016/J.JNONCRYSOL.2004.08.264

87. Urata S, Hijiya H, Niwano K, Matsui J. Theoretical estimation of dielectric loss of oxide glasses using nonequilibrium molecular dynamics simulations. *J Am Ceram Soc*. 2022;105:4200–4207. https://doi.org/10.1111/jace.18411

88. Urata S, Sato Y. A study on the plasticity of soda-lime silica glass via molecular dynamics simulations; A study on the plasticity of soda-lime silica glass via molecular dynamics simulations. *J Chem Phys*. 2017;147:174501. https://doi.org/10.1063/1.4997293

89. McMillan PF, Wolf GH. Vibrational spectroscopy of silicate liquids. 1st ed. *Struct. Dyn. Prop. Silic. Melts*, 1st ed. Vol. 32. 2019:247–315.

90. Charles RJ. Polarization and Diffusion in a Silicate Glass ARTICLES YOU MAY BE INTERESTED IN. *J Appl Phys*. 1961;32:1115. https://doi.org/10.1063/1.1736169

91. King PL, McMillian PF, Moore GM. Infrared spectroscopy of silicate glasses with application to natural systems. London: Mineralogical Association of Canada; 2004

92. Kob W, Andersen HC. Testing mode-coupling theory for a supercooled binary Lennard-Jones mixture I: The van Hove correlation function. *Phys Rev E*. 1995;51(5):4626. https://doi.org/10.1103/PhysRevE.51.4626

93. Lodesani F, Menziani MC, Hijiya H, Takato Y, Urata S, Pedone A. Structural origins of the Mixed Alkali Effect in Alkali Aluminosilicate Glasses: Molecular Dynamics Study and its Assessment. *Sci Reports 2020 101*. 2020;10(1):1–18. https://doi.org/10.1038/s41598-020-59875-7

94. Onodera Y, Takimoto Y, Hijiya H, *et al.* Origin of the mixed alkali effect in silicate glass. *NPG Asia Mater*. 2019;11(1). https://doi.org/10.1038/s41427-019-0180-4

95. Uhlig H, Hoffmann MJ, Lamparter HP, Aldinger F, Bellissent R, Steeb S. Short-range and medium-range order in lithium silicate glasses, Part I: Diffraction experiments and results. *J Am Ceram Soc*. 1996;79(11):2833–2838. https://doi.org/10.1111/J.1151-2916.1996.TB08716.X

96. Huang C, Cormack AN. The structure of sodium silicate glass. *J Chem Phys*. 1998;93(11):8180. https://doi.org/10.1063/1.459296

97. Huang C, Cormack AN. Structural differences and phase separation in alkali silicate glasses. *J Chem Phys*. 1998;95(5):3634. https://doi.org/10.1063/1.460814

98. Inaba S, Fujino S, Morinaga K. Young's modulus and compositional parameters of oxide glasses. *J Am Ceram Soc*. 1999;82(12):3501–3507. https://doi.org/10.1111/J.1151-2916.1999.TB02272.X

99. Shannon RD. Revised Effective Ionic Radii and Systematic Studies of Interatomie Distances in Halides and Chaleogenides. *Acta Cryst*. 1976;32:751.

100. Davis MC, Kaseman DC, Parvani SM, *et al.* Q(n) species distribution in K2Oa2SiO2 glass by

29Si magic angle flipping NMR. *J Phys Chem A*. 2010;114(17):5503–5508. https://doi.org/10.1021/JP100530M

101. Zhang P, Dunlap C, Grandinetti P, Farnan I, Stebbins J. Silicon site distributions in an alkali silicate glass derived by two-dimensional 295i nuclear magnetic resonance. *J Non Cryst Solids*. 1996;204:294–300.

102. Sen S, Youngman RE. NMR study of Q-speciation and connectivity in K 2 O-SiO 2 glasses with high silica content. n.d. https://doi.org/10.1016/j.jnoncrysol.2003.08.071

103. Maekawa H, Maekawa T, Kawamura K, Yokokawa T. The structural groups of alkali silicate glasses determined from 29Si MAS-NMR. *J Non Cryst Solids*. 1991;127:53–64.

104. Celia I. Merzbacher; William B. White. Structure of Na in aluminosilicate glasses; a far-infrared reflectance spectroscopic study. *Am Mineral*. 1988;73:1089–1094.

105. Kjeldsen J, Smedskjaer MM, Mauro JC, Youngman RE, Huang L, Yue Y. Mixed alkaline earth effect in sodium aluminosilicate glasses. 2013. https://doi.org/10.1016/j.jnoncrysol.2013.03.015

106. Roling B, Ingram MD. Mixed alkaline-earth effects in ion conducting glasses. *J Non Cryst Solids*. 2000;265(1):113–119. https://doi.org/10.1016/S0022-3093(99)00899-6

107. Isard JO. The mixed alkali effect in glass. *J Non Cryst Solids*. 1969;1(3):235–261. https://doi.org/10.1016/0022-3093(69)90003-9

108. Day DE. Mixed alkali glasses - Their properties and uses. *J Non Cryst Solids*. 1976;21(3):343–372. https://doi.org/10.1016/0022-3093(76)90026-0

109. Balasubramanian S, Rao KJ. LETTERS Preferential Paths in Alkali Ion Migration and the Mixed Alkali Effect in Silicate Glassest. *NUMBER*. 1993;97.

110. DUKE DA, MacDowell JF, KARSTETTER BR. Crystallization and Chemical Strengthening of Nepheline Glass-Ceramics. *J Am Ceram Soc*. 1967;50(2):67–74. https://doi.org/10.1111/j.1151-2916.1967.tb15041.x

111. Natrup F V., Bracht H, Murugavel S, Roling B. Cation diffusion and ionic conductivity in soda-lime silicate glasses. *Phys Chem Chem Phys*. 2005;7(11):2279–2286. https://doi.org/10.1039/B502501J

112. Lima MM, Monteiro R. Characterisation and thermal behaviour of a borosilicate glass. *Thermochim Acta*. 2001;373(1–2):69–74. https://doi.org/10.1016/S0040-6031(01)00456-7

113. Dell WJ, Bray PJ, Xiao SZ. It B NMR STUDIES AND STRUCTURAL MODELING OF Na20-B203-SiO 2 GLASSES OF HIGH SODA CONTENT *. *J Non Cryst Solids*. 1983;58:1–16.

114. Le Losq C, Neuville DR, Florian P, Henderson GS, Massiot D. The role of Al 3+ on rheology and structural changes in sodium silicate and aluminosilicate glasses and melts. n.d. https://doi.org/10.1016/j.gca.2013.11.010

115. Hsieh CH, Jain H, Miller AC, Kamitsos EI. X-ray photoelectron spectroscopy of Al- and B-substituted sodium trisilicate glasses. *J Non Cryst Solids*. 1994;168(3):247–257.

https://doi.org/10.1016/0022-3093(94)90336-0

116. Kamitsos EI, Kapoutsis JA, Jain H, Hsieh CH. Vibrational study of the role of trivalent ions in sodium trisilicate glass. *J Non Cryst Solids*. 1994;171(1):31–45. https://doi.org/10.1016/0022-3093(94)90030-2

117. Parker TE, Schulz MB. SiO2 film overlays for temperature‒stable surface acoustic wave devices. *Appl Phys Lett*. 1975;26(3):75–77. https://doi.org/10.1063/1.88076

118. Matsuda S, Miura M, Matsuda T, Ueda M, Satoh Y, Hashimoto K. Investigation of SiO2 film properties for zero temperaturecoefficient of frequency SAW devices. *Proc - IEEE Ultrason Symp*. 2010;633–636. https://doi.org/10.1109/ULTSYM.2010.5935494

119. Miura M, Matsuda T, Satoh Y, *et al.* Temperature compensated LiTaO3/sapphire bonded SAW substrate with low loss and high coupling factor suitable for US-PCS application. *Proc - IEEE Ultrason Symp*. 2004;2:1322–1325. https://doi.org/10.1109/ULTSYM.2004.1418036

120. Ohsato H. Functional advances of microwave dielectrics for next generation. *Ceram Int*. 2012;38(SUPPL. 1):S141–S146. https://doi.org/10.1016/J.CERAMINT.2011.04.068

121. Sugimoto Y, Mori N, Moriya Y, Takada T. Dielectric properties of new LTCC material applied to high frequencies. n.d. https://doi.org/10.2109/jcersj2.122.P6-1

122. SHELBY JE. Formation and Properties of Calcium Aluminosilicate Glasses. *J Am Ceram Soc*. 1985;68(3):155–158. https://doi.org/10.1111/J.1151-2916.1985.TB09656.X

123. Bansal NP, Doremus RH. Handbook of Glass Properties. *Handb Glas Prop*. 2013;1–680. https://doi.org/10.1016/C2009-0-21785-5

124. Wu JM, Huang HL. Microwave properties of zinc, barium and lead borosilicate glasses. *J Non Cryst Solids*. 1999;260(1–2):116–124. https://doi.org/10.1016/S0022-3093(99)00513-X

125. González De Arrieta I, González-Fernández L, Echániz T, Del Campo L, De Sousa Meneses D, López GA. Small-polaron-induced infrared opacification in rutile TiO2. *J Appl Phys*. 2021;130(7). https://doi.org/10.1063/5.0056081/158186

126. Ohsato H, Kato H, Mizuta M, Nishigaki S, Okuda T. Microwave dielectric properties of the ba6-3x(sm1-y,\mbry)8C2xti18o54 (\mbr=nd and la) solid solutions with zero temperature coefficient of the resonant frequency. *Jpn J Appl Phys*. 1995;34(9):5413–5417. https://doi.org/10.1143/JJAP.34.5413/XML

127. Ohsato H, Ohsato H. Microwave Dielectrics with Perovskite-Type Structure. *Perovskite Mater - Synth Characterisation, Prop Appl*. 2016. https://doi.org/10.5772/61718

128. Hlinka J, Ostapchuk T, Nuzhnyy D, *et al.* Coexistence of the Phonon and Relaxation Soft Modes in the Terahertz Dielectric Response of Tetragonal BaTiO 3. 2008. https://doi.org/10.1103/PhysRevLett.101.167402

129. Sawaguchi E, Kikuchi A, Kodera Y. Dielectric Constant of Strontium Titanate at Low Temperatures. *J Phys Soc Japan*. 1962;17(10):1666–1667. https://doi.org/10.1143/JPSJ.17.1666

130. BEALL GH, KARSTETTER BR, RITTLER HL. Crystallization and Chemical Strengthening of Stuffed β-Quartz Glass-Ceramics. *J Am Ceram Soc*. 1967;50(4):181–190. https://doi.org/10.1111/J.1151-2916.1967.TB15077.X

131. DOHERTY PE, LEE DW, DAVIS RS. Direct Observation of the Crystallization of Li2O-Al2O3-SiO2 Glasses Containing TiO2. *J Am Ceram Soc*. 1967;50(2):77–81. https://doi.org/10.1111/J.1151-2916.1967.TB15043.X

132. Stookey SD. Catalyzed Crystallization of Glass in Theory and Practice. *Ind Eng Chem*. 1959;51(7):805–808. https://doi.org/10.1021/IE50595A022/ASSET/IE50595A022.FP.PNG_V03

133. Höland W, Beall GH. Glass-ceramic technology. 2019 https://doi.org/10.1002/9781119423737

134. Kanehara K, Hoshina T, Takeda H, Tsurumi T. Terahertz permittivity of rutile TiO2 single crystal measured by anisotropic far-infrared ellipsometry. *J Ceram Soc Japan*. 2015;123(1437):303–306. https://doi.org/10.2109/JCERSJ2.123.303

135. Izumi F, Momma K. Three-Dimensional Visualization in Powder Diffraction. *Solid State Phenom*. 2007;130:15–20. https://doi.org/10.4028/WWW.SCIENTIFIC.NET/SSP.130.15

136. Petzelt J, Nuzhnyy D, Bovtun V, Crandles DA. Origin of the colossal permittivity of (Nb + In) co-doped rutile ceramics by wide-range dielectric spectroscopy. *Phase Transitions*. 2018;91(9–10):932–941. https://doi.org/10.1080/01411594.2018.1501801

137. Aspnes DE. Local-field effects and effective-medium theory: A microscopic perspective. *Am J Phys*. 1982;50(8):704–709. https://doi.org/10.1119/1.12734

138. Takahashi S, Imai Y, Kan A, Hotta Y, Ogawa H. Dielectric and thermal properties of isotactic polypropylene/hexagonal boron nitride composites for high-frequency applications. *J Alloys Compd*. 2014;615:141–145. https://doi.org/10.1016/J.JALLCOM.2014.06.138

139. Li L, Fang Y, Xiao Q, Wu YJ, Wang N, Chen XM. Microwave Dielectric Properties of Fused Silica Prepared by Different Approaches. *Int J Appl Ceram Technol*. 2014;11(1):193–199. https://doi.org/10.1111/J.1744-7402.2012.02846.X